

The Clever Hans Effect in Unsupervised Learning

Jacob Kauffmann^{1,2}, Jonas Dippel^{1,2,3}, Lukas Ruff^{1,3}, Wojciech Samek^{1,2,5},
Klaus-Robert Müller^{1,2,6,7,8,*} and Grégoire Montavon^{4,2,1,*}

¹Department of Electrical Engineering and Computer Science, Technische Universität Berlin, Germany

²BIFOLD – Berlin Institute for the Foundations of Learning and Data, Berlin, Germany

³Aignostics, Berlin, Germany

⁴Department of Mathematics and Computer Science, Freie Universität Berlin, Germany

⁵Department of Artificial Intelligence, Fraunhofer HHI, Berlin, Germany

⁶Department of Artificial Intelligence, Korea University, Seoul, Korea

⁷Max-Planck Institute for Informatics, Saarbrücken, Germany

⁸Google Deepmind, Berlin, Germany

* Corresponding authors (email: klaus-robot.mueller@tu-berlin.de, gregoire.montavon@fu-berlin.de)

Abstract

Unsupervised learning has become an essential building block of AI systems. The representations it produces, e.g. in foundation models, are critical to a wide variety of downstream applications. It is therefore important to carefully examine unsupervised models to ensure not only that they produce accurate predictions, but also that these predictions are not “right for the wrong reasons”; the so-called Clever Hans (CH) effect. Using specially developed Explainable AI techniques, we show for the first time that CH effects are widespread in unsupervised learning. Our empirical findings are enriched by theoretical insights, which interestingly point to inductive biases in the unsupervised learning machine as a primary source of CH effects. Overall, our work sheds light on unexplored risks associated with practical applications of unsupervised learning and suggests ways to make unsupervised learning more robust.

Unsupervised learning is a subfield of machine learning that has gained prominence in recent years [1–3]. It addresses fundamental limitations of supervised learning, such as the lack of labels in the data or the high cost of acquiring them. Unsupervised learning has achieved successes in modeling the unknown, such as uncovering new cancer subtypes [4, 5] or extracting novel insights from large historical corpora [6]. Furthermore, the fact that unsupervised learning does not rely on task-specific labels makes it a good candidate for core AI infrastructure: Unsupervised anomaly detection provides the basis for various quality or integrity checks on the input data [7–10]. Unsupervised learning is also a key technology behind ‘foundation models’ [1, 11–15] which extract representations upon which various downstream models (e.g. classification, regression, ‘generative AI’, etc.) can be built. The growing popularity of unsupervised learning models creates an urgent need to carefully examine how they arrive at their predictions. This is essential to ensure that potential flaws in the way these models process and represent the input data are not propagated to the many downstream supervised models that build upon them.

In this paper, we show for the first time that unsupervised learning models largely suffer from Clever Hans (CH) effects [16], also known as “right for the wrong reasons”. Specifically, we find that unsupervised learning models often produce representations from which instances can be correctly predicted to be e.g. similar or anomalous, although largely supported

by data quality artifacts. The flawed prediction strategy is not detectable by common evaluation benchmarks such as cross-validation, but may manifest itself much later in ‘downstream’ applications in the form of unexpected errors, e.g. if subtle changes in the input data occur after deployment (cf. Fig. 1). While CH effects have been studied quite extensively for *supervised learning* [16–20], the lack of similar studies in the context of *unsupervised learning*, together with the fact that unsupervised models supply many downstream applications, is a cause for concern.

For example, in industrial inspection, which often relies on unsupervised anomaly detection [9, 10], we find that a CH decision strategy can systematically miss a wide range of manufacturing defects, resulting in potentially significant costs. As another example, unsupervised foundation models, advocated in the medical domain to provide robust features for various specialized diagnostic tasks, can potentially introduce CH effects into many of these tasks, with the prominent risk of large-scale misdiagnosis. These scenarios (illustrated in Fig. 1) highlight the practical implications of an unsupervised CH effect, which, unlike its supervised counterpart, may not be limited to malfunctioning in a single specific task, but potentially in all downstream tasks.

To uncover and understand unsupervised Clever Hans effects, we propose to use Explainable AI [21–25] (here techniques that build on the LRP explanation framework [26–28]). Our proposed use of these techniques allows us to

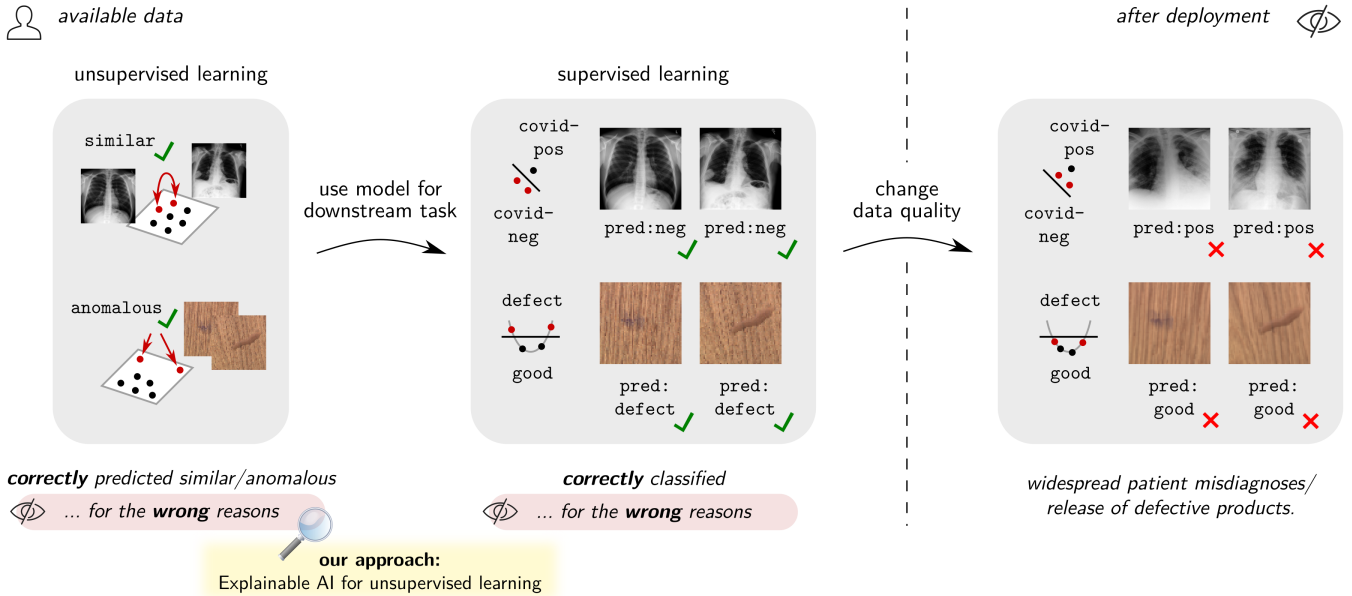


Figure 1: The CH effect in unsupervised learning. The unsupervised model correctly represents data instances as similar or anomalous, but for the wrong reasons, e.g. based on irrelevant input features such as artifacts. The problem is critical because the flaw can be inherited by potentially many downstream tasks. The CH effect typically goes undetected in a classical validation procedure and manifests itself in the form of prediction errors only after deployment.

identify at scale which input features are used (or misused) by the unsupervised ML model, without having to formulate specific hypotheses or downstream tasks. Specifically, we use an extension of LRP called BiLRP [6] to reveal input patterns that are jointly responsible for similarity in the representation space. We also combine LRP with ‘virtual layers’ [29, 30] to reveal pixel and frequency components that are jointly responsible for predicted anomalies.

Furthermore, our Explainable AI-based analysis allows us to pinpoint more formal causes for the emergence of unsupervised CH effects. In particular, they are due not so much to the *data*, but to the *unsupervised learning machine*, which hinders the integration of the true task-supporting features into the model, even though vast amounts of data points are available. Our findings provide a novel direction for developing targeted strategies to mitigate CH effects and increase model robustness.

Overall, our work sheds light on the presence, prominence, and distinctiveness of CH effects in unsupervised learning, calling for increased scrutiny of this essential component of modern AI systems.

Results

Using Explainable AI, we investigate the emergence of Clever Hans effects in a representative set of unsupervised learning tasks, including representation learning and anomaly detection.

Clever Hans Effects in Representation Learning

We first consider an application of representation learning in the context of detecting COVID-19 cases from X-ray scans [31, 32]. Simulating an early pandemic phase characterized by data scarcity, similar to [32], we use a dataset aggregation approach where a large, well-established non-COVID-19 dataset is merged with a more recent COVID-19 dataset aggregated from multiple sources. Specifically, we aggregate 2597 instances of the CXR8 dataset [33] from the National Institute of Health (NIH), collected between 1992 and 2015, with the 535 instances of the GitHub-hosted ‘COVID-19 image data collection’ [34]. We refer to these subsets as ‘NIH’ and ‘GitHub’, respectively.

Further motivated by the need to accommodate the critically small number of COVID-19 instances in the aggregated dataset and to avoid overfitting, we choose to rely on the representations provided by unsupervised foundation models [15, 35–37]. Specifically, we feed our data into a pre-trained PubMedCLIP model [36], which has built its representation from a very large collection of X-ray scans in an unsupervised manner. Based on the PubMedCLIP representation, we train a downstream classifier that separates COVID-19 from non-COVID-19 instances with a class-balanced accuracy of 88.6% on the test set (cf. Table 1). However, a closer look at the structure of this performance score reveals a strong disparity between the NIH and GitHub subgroups, with all NIH instances being correctly classified and the

GitHub instances having a lower class-balanced accuracy of 75.2%, and, more strikingly, a false positive rate (FPR) of 40%, as shown in Table 1. Considering that the higher heterogeneity of instances in the GitHub dataset is more characteristic of real-world conditions, such a high FPR prohibits any practical use of the model as a diagnostic tool. We emphasize that this deficiency could have been easily overlooked if one did not pay close attention to (or did not know) the data sources, and instead relied only on the overall accuracy score.

To proactively detect this heterogeneous, non-robust prediction behavior and to test whether it originates from the unsupervised PubMedCLIP component, we propose to use Explainable AI. Using the BiLRP [6] technique, we investigate whether PubMedCLIP represents different instances as similar based on a correct strategy or a ‘Clever Hans’ strategy. The BiLRP method is illustrated in Fig. 2 and its mathematical formulation is given in the Methods section. The output of BiLRP for two exemplary pairs of COVID-positive instances is shown in Fig. 3 (left). The BiLRP explanation shows that the modeled similarity between pairs of COVID-positive instances comes from text-like annotations that appear in both images. This is a clear case of a CH effect, where the modeled similarity is *right* (instances share being COVID-positive), but for the *wrong reasons*

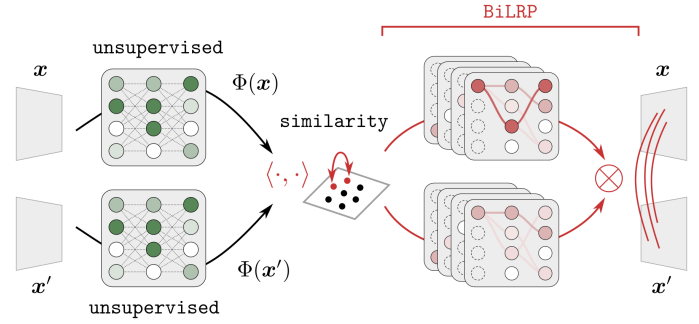


Figure 2: Illustration of the BiLRP method for explaining similarity predictions of a representation learning model. The output of BiLRP is a decomposition of the predicted similarity onto pairs of features from the two input images. It is typically displayed as a weighted bipartite graph connecting the contributing feature pairs.

(similarity is based on shared textual annotations). The unmasking of this CH effect by BiLRP warns of the risk that downstream models based on these similarities (and more generally on the flawed representation) may inherit the CH effect. This a posteriori explains the excessively high (40%) FPR of the downstream classifier on the Github subset, as the model’s reliance on text makes it difficult to separate Github’s COVID-positive from COVID-negative

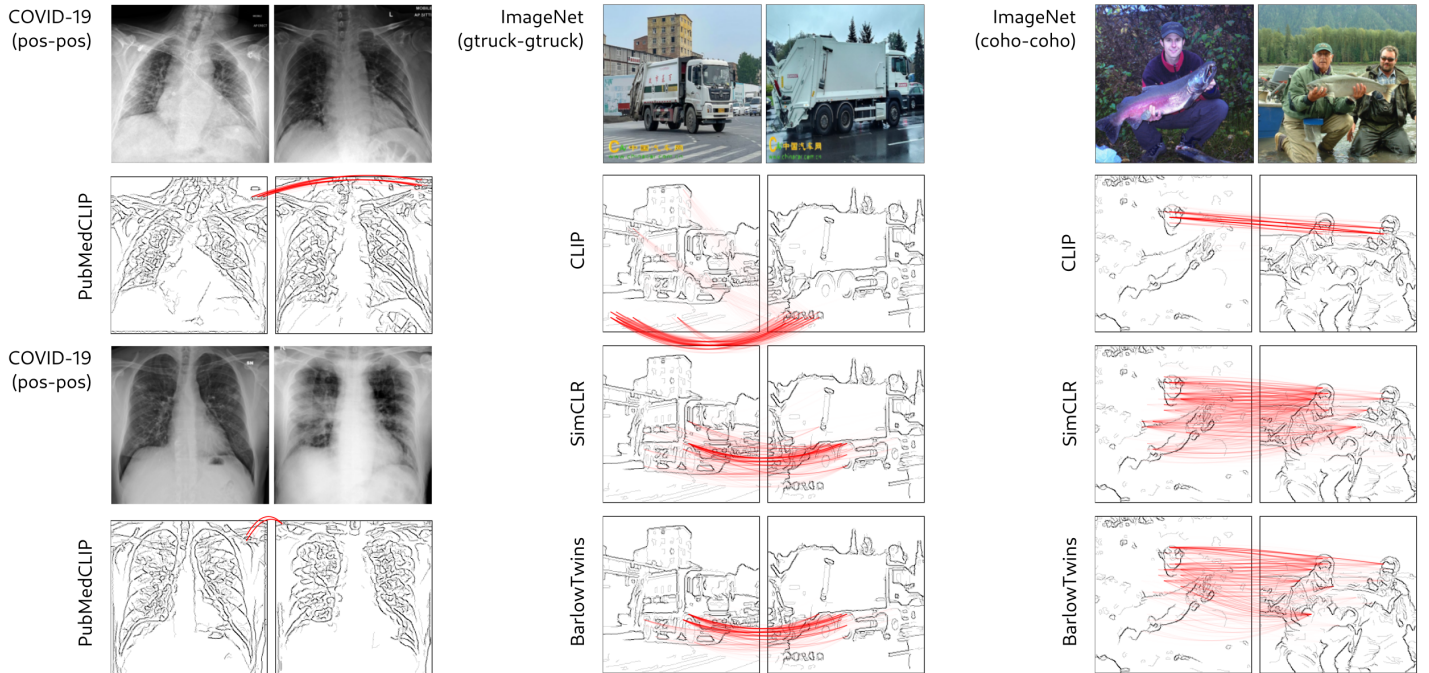


Figure 3: BiLRP analysis of the PubMedCLIP unsupervised model and the general-purpose CLIP, SimCLR, and BarlowTwins unsupervised models. The analysis reveals a variety of CH strategies, specifically instances that are correctly represented as similar by the unsupervised model but for the wrong reasons. Similarity between COVID-positive instances arises from shared spurious textual annotations. Similarly, on ImageNet data, unsupervised models incorrectly rely on logo artifacts or the presence of humans in the background for their similarity predictions.

instances (cf. Supplementary Note A for further analysis). We note that, unlike the per-group accuracy analysis above, our BiLRP analysis did not require provenance metadata (GitHub or NIH), nor did it focus on a specific downstream task with its specific labels.

To test whether representation learning has a general tendency to evolve CH strategies beyond the above use case, we downloaded three generic foundation models, namely the original CLIP model [13], SimCLR [12, 38] and BarlowTwins [39]. As a downstream task, we consider the classification, using linear-softmax classifiers, of the 8 classes from ImageNet [40] that share the WordNet ID ‘truck’ and of the 16 ImageNet classes that share the WordNet ID ‘fish’ (see the Methods section for details). The test accuracy of each model on these two tasks is given in Table 1 (columns ‘original’). On the truck classification task, the CLIP model performs best, with an accuracy of 85.0%. On the fish classification task, the CLIP and supervised models perform best, with accuracies of 86.5% and 86.2%, respectively.

We use BiLRP to examine the representations of these unsupervised models. In Fig. 3 (center), we observe that CLIP-based similarities, as in PubMedCLIP, also rely on text. Here, a textual logo in the lower left corner of two garbage truck images is used to support similarity¹. In contrast, SimCLR and BarlowTwins instead rely on the actual garbage truck, demonstrating that CH effects are specific to the unsupervised learning technique. In Fig. 3 (right), we observe that *all* unsupervised models focus on humans and are unresponsive to fish features. CLIP focuses specifically on facial features. While the detection of human features may be useful for many downstream tasks, the suppression of fish features strongly exposes other downstream fish classification tasks to even mild spurious correlations, systematically leading to CH behavior.

The heterogeneity of strategies across models revealed by BiLRP suggests that, in addition to inhomogeneities in the unsupervised data, biases induced by the unsupervised pre-training algorithm² play an important role in the formation of CH effects. The spurious amplification of humans in the center of the image observed for SimCLR and BarlowTwins can be attributed to the cropping mechanism these methods implement, where human features in the center are sufficient and robust to solve the SimCLR and BarlowTwins similarity tasks. In the case of CLIP (and PubMedCLIP), the systematic amplification of textual, facial, or other identifying features can be explained by the fact that these features often provide useful information for CLIP’s unsupervised image-text matching task.

The consequences of these Clever Hans effects are shown

¹ The reliance on logos for the garbage truck class has been highlighted in previous work in the context of supervised learning [18].

² See also [41–44] for further analyses of these biases.

quantitatively in Table 1. We observe a systematic degradation of performance when moving from the original data to data subsets where the presence/absence of an artifact is no longer predictive of the class. In particular, for the truck data, we observe a sharp drop in the accuracy of the CLIP model from 85.0% on the original data to 80.5% on the same data with a logo inserted on each image (column ‘logo’ in Table 1). For the fish data, a similar drop in accuracy is observed for SimCLR and BarlowTwins from 82.2% and 83.1% respectively on the original data to 78.6% and 75.6% respectively when only images containing humans are retained and class rebalancing is performed. This shows that the CH effects detected by our BiLRP analysis have concrete negative practical consequences in terms of the ability of unsupervised models and downstream classifiers to predict uniformly well across subgroups and to generalize. In comparison, the baseline supervised model generally shows more stable performance between the original data and the newly defined subsets. A detailed analysis of the structure of the prediction errors for each classification task, supported by confusion matrices, is given in Supplementary Note B.

Clever Hans Effects in Anomaly Detection

Extending our investigation of the CH effect to another instance of unsupervised learning, namely anomaly detection, we consider an industrial inspection use case based on the popular MVTEC-AD dataset [9]. The dataset consists of 15 product categories, each consisting of a training set of images without manufacturing defects and a test set of images with and without defects. Since manufacturing defects are infrequent and heterogeneous in nature, the problem is typically approached using unsupervised anomaly detection [2, 9]. These models map each instance to an anomaly score, from which threshold-based downstream models can be built to classify between instances with and without manufacturing defects. Unsupervised anomaly detection has received considerable attention, with sophisticated approaches based on deep neural networks such as PatchCore [45] or EfficientAD [46], showing excellent performance in detecting a wide range of industrial defects.

Somewhat surprisingly, simpler approaches based on distances in pixel space show comparatively high performance for selected tasks [2]. We consider one such approach, which we call ‘D2Neighbors’, where anomalies are predicted according to the distance to neighbors in the training data. Specifically, the anomaly score of an instance \mathbf{x} is computed as $f(\mathbf{x}) = \text{softmin}_j \{\|\mathbf{x} - \mathbf{u}_j\|^2\}$ where $(\mathbf{u}_j)_{j=1}^N$ is the set of available inlier instances (see the Methods section for details on the model and data preprocessing). This anomaly model belongs to the broader class of distance-based models [47–49], and connections can be made to kernel density estimation

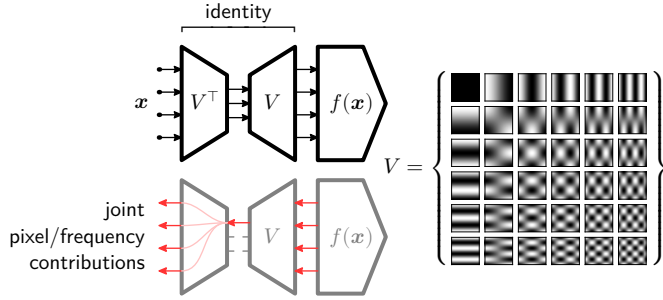


Figure 4: Schematic of the virtual inspection layer used to explain anomalies in the joint pixel-frequency domain. To map pixels to frequencies and back, we use the discrete cosine transform (DCT), whose basis elements are shown on the right.

[50, 51] and one-class SVMs [52]. Using D2Neighbors, we are able to build downstream models that classify industrial defects of the MVTec data with F1-scores above 0.9 for five categories (bottle, capsule, pill, toothbrush, and wood).

To shed light on the prediction strategy that leads to these unexpectedly high F1-scores, we investigate the underlying D2Neighbors anomaly model using Explainable AI. Specifically, we consider an extension of LRP for anomaly detection [28, 53] and further equip the explanation technique with ‘virtual layers’ [29, 30]. The technique of ‘virtual layers’ (cf. Fig. 4) is to map the input to an abstract domain and back, leaving the prediction function *unchanged*, but providing a new representation in terms of which the prediction can be explained. We construct such a layer by applying the discrete cosine transform (DCT) [54], shown in Fig. 4 (right), followed by its inverse. This allows us to explain the predictions *jointly* in terms of pixels and frequencies.

The result of our proposed analysis is shown in Fig. 5 for instances from two of the five retained MVTec categories (see Supplementary Note C for more instances). Explanations at the *pixel* level show that D2Neighbors supports its anomaly predictions largely based on pixels containing the actual industrial defect. The squared difference in its distance function ($\|\Delta\|^2 = \sum_i \Delta_i^2$) encourages a sparse pixel-wise response of the model, efficiently discarding regions of the image where the new instance shows no difference from instances in the training data. However, we also see in the pixel-wise explanation that a non-negligible part of the anomaly prediction comes from irrelevant background pixels. Joint *pixel-frequency* explanations shed light on these unresolved contributions, showing that they arise mostly from the high-frequency part of the model’s decision strategy (Fig. 5 B and C).

The exposure of the model to these irrelevant high-frequency features, as detected by our LRP analysis, raises concerns about the robustness of the model under changing data conditions (e.g. after the model is deployed). We experiment with an innocuous perturbation of the data conditions, which consists of changing the image resizing algorithm from OpenCV’s nearest neighbor resizing to a more sophisticated resizing method that includes antialiasing. Resizing techniques have been shown in some cases to significantly affect image quality and ML model prediction [55], but their effect on ML models, especially unsupervised ones, has been little studied. The performance of the D2Neighbors model and other models before and after changing the resizing algorithm is shown in Table 1 (columns ‘original’ and ‘deployed’ respectively). The F1 score performance of D2Neighbors degrades significantly from 0.92 to 0.80. In particular, there is

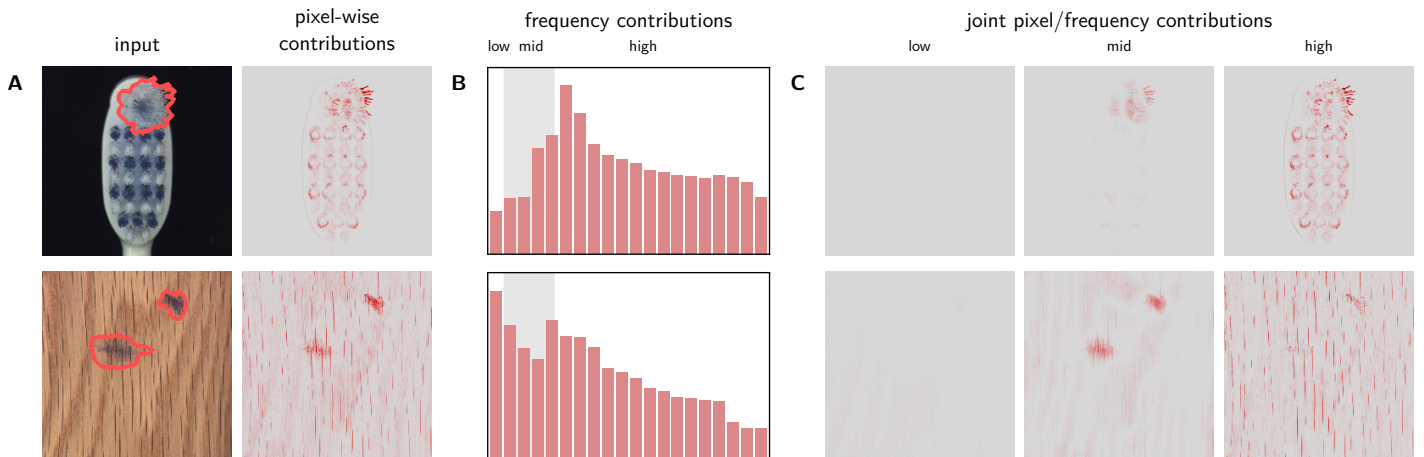


Figure 5: Explainable AI analysis of the D2Neighbors anomaly model. **A:** Selected images from MVTec-AD (ground truth anomaly shown as red contour) and a pixel-wise LRP explanation of the anomaly prediction. Explanations for other categories are given in Supplementary Note C. **B:** Frequency domain explanations (averaged over all anomalous test instances). The x-axis represents the frequencies (on a power scale), and the y-axis is the contribution of the corresponding frequencies to the anomaly prediction. **C:** Pixel-wise contributions filtered by frequency band.

a large increase in the false negative rate (FNR) from 4% to 26% (cf. Table 1). In an industrial inspection setting, an increase in FNR has serious consequences, in particular, many defective instances are missed and propagated through the production chain, resulting in wasted resources in subsequent production stages and high recall costs. This performance degradation of D2Neighbors in post-deployment conditions is particularly surprising given that data quality has actually *improved*. This is a direct consequence of the CH strategy we identified, namely D2Neighbors’ reliance on high frequencies. When antialiasing is introduced into the resizing procedure, the high frequencies that the D2Neighbors model uses to support its prediction disappear from the data, and this significantly reduces the anomaly scores of each instance, thereby increasing the FNR.

Interestingly, the performance degradation of D2Neighbors is even more severe when the ℓ_2 -norm in the distance function is replaced by the ℓ_1 -norm (cf. Table 1). This can be explained by the fact that the ℓ_1 -norm, unlike the ℓ_2 -norm, does not implement pixel-wise sparsity and is therefore more exposed to irrelevant input regions. Conversely, the application of an ℓ_4 -norm results in sensibly higher robustness than the original ℓ_2 -norm. We note that even the more sophisticated PatchCore model [45] (cf. Methods section), which integrates several robustness mechanisms including preprocessing layers and spatial max-pooling, is not fully immune to irrelevant high-frequency components and also shows a noticeable performance degradation in post-deployment conditions (cf. Table 1).

Overall, our experiments show that performance on the available test data is an insufficient indicator of the quality of an anomaly detector. Its robustness to changes in the quality of the input data cannot be guaranteed. This can

be diagnosed by Explainable AI and a careful subsequent inspection of the structure of the anomaly model.

Alleviating CH in Unsupervised Learning

Leveraging the Explainable AI analysis above, we aim to build models that are more robust across different data subgroups and in post-deployment conditions. Unlike previously proposed CH removal techniques [18, 19], we aim to operate on the unsupervised model rather than the downstream tasks. This potentially allows us to achieve broad robustness improvements while leaving the downstream learning machines (training supervised classifiers or adjusting detection thresholds) untouched.

We first test our CH mitigation approach on the CLIP model, which our Explainable AI analysis has shown to incorrectly rely on text. Specifically, we focus on an early layer of the CLIP model (encoder.relu3) and remove the feature maps that are most responsive to text. We then apply a similar CH mitigation approach to anomaly detection, which our Explainable AI analysis has shown to be overexposed to high frequencies. Here, we propose to prune the high frequencies by inserting a blur layer at the input of the model.

In both cases, the proposed CH mitigation technique provides strong benefits in terms of model robustness. As shown in Table 1, rows ‘CH mitigation’, our robustified models substantially reverse the performance degradation observed in post-deployment conditions, reaching performance levels close to, and in some cases superior to, those measured on the original data.

	COVID-19		ImageNet:truck		ImageNet:fish		MVTec-AD*		
	<i>original</i>	github	<i>original</i>	logo	<i>original</i>	human		<i>original</i>	deployed
PubMedCLIP	88.6	75.2 ↓	—	—	—	—	D2Neighbors (ℓ_2)	0.92	0.80 ↓
	FPR: 14%	FPR: 40%						FNR: 4%	FNR: 26%
CLIP	—	—	85.0	80.5 ↓	86.5	83.8	+ CH mitigation	0.94	0.93 ↑
+ CH mitigation	—	—	85.2	85.0 ↑	—	—	PatchCore	0.92	0.85 ↓
SimCLR	—	—	74.8	74.5	82.2	78.6 ↓	+ CH mitigation	0.97	0.96 ↑
BarlowTwins	—	—	80.2	80.2	83.1	75.6 ↓	D2Neighbors (ℓ_1)	0.93	0.74 ↓
<i>Supervised</i>	—	—	83.8	83.2	86.2	84.2	D2Neighbors (ℓ_4)	0.91	0.83 ↓

Table 1: Performance of unsupervised models on different data subsets or conditions. Left: Class-balanced classification accuracy of downstream models (COVID-19, truck and fish classification) built on different unsupervised representation learning models. Accuracy scores are reported for the original test set and for a subset containing specific instances. Right: F1 scores of different anomaly detection models. Performance is reported on the simulated original and post-deployment data conditions (standard and antialiased resizing, respectively). (*) Performance on MVTec-AD is computed for each of the 5 classes retained for the analysis and averaged. (↓) Severe performance degradation (of 3 percentage points or more) after deployment. (↑) Major performance improvement (of 3 percentage points or more) after CH mitigation.

Discussion

Unsupervised learning is an essential category of ML that is increasingly used in core AI infrastructure to power a variety of downstream tasks, including generative AI. Much research to date has focused on improving the performance of unsupervised learning algorithms, for example, to maximize accuracy scores in downstream classification tasks. These evaluations often pay little attention to the exact strategy used by the unsupervised model to achieve the reported high performance, in particular whether these models rely on Clever Hans strategies.

Building on recent techniques from Explainable AI, we have shown for the first time that CH strategies are prevalent in several unsupervised learning paradigms. These strategies can take various forms, such as correctly predicting the similarity of two X-ray scans based on irrelevant shared annotations, or predicting that an image is anomalous based on small but widespread pixel-level artifacts. These flawed prediction strategies result in models that do not transfer well to changing conditions at test time. Most importantly, their lack of robustness infects many downstream models that rely on them. As we have shown in two use cases, this can lead to widespread misdiagnosis of patients or failure to detect manufacturing defects.

Therefore, addressing CH effects is a critical step towards reliable use of unsupervised learning methods. However, compared to a purely task-specific supervised approach, the addition of an unsupervised component, potentially serving multiple downstream tasks, adds another dimension of complexity to the modeling problem. In particular, one must decide whether to handle CH effects in the downstream classifier or *directly* in the unsupervised model part. Approaches consisting of dynamically updating downstream models in response to changing conditions [56–59], or revising their decision strategies with human feedback [18, 19, 60] are possible solutions to maintain high accuracy. However, these approaches may not be sustainable because CH mitigation must be performed repeatedly for each new downstream task. The problem may persist even after a flaw in the foundation model becomes known (e.g. [61, 62]), due to release intervals and the high cost of retraining these models. Instead, our results argue for addressing CH effects directly when building the unsupervised model, with the goal of achieving persistent robustness that benefits existing and future downstream applications.

Using advanced Explainable AI techniques targeted at unsupervised learning, we have uncovered multiple and diverse CH effects, such as the reliance of CLIP (and its derivative PubMedCLIP) on textual annotations, or a systemic over-exposure of unsupervised anomaly models to noise. Interestingly, our analysis has revealed that these

unsupervised CH effects differ from supervised ones in that they arise less from the data and more from inductive biases in the model and learning algorithm. These include spurious suppression/amplification effects caused by the representation learning’s training objective, or a failure of unsupervised anomaly detection architectures to replicate frequency filtering mechanisms found in supervised learning [63–65], leaving the learned models highly exposed to noise. Furthermore, our Explainable AI analysis not only provided new insights into the formal causes of unstable behavior in unsupervised learning. Our experiments also showed how pruning the high-frequency or spuriously amplified features revealed by our Explainable AI analysis leads to systematic performance improvements on difficult data subgroups or in post-deployment conditions. In doing so, we have demonstrated the actionability of our Explainable AI approach, showing that it can guide the process of identifying and subsequently correcting the faulty components of an unsupervised learning model.

While our investigation of unsupervised CH effects and their consequences has focused on image data, extension to other data modalities seems straightforward. Explainable AI techniques such as LRP, which are capable of accurate dataset-wide explanations, operate independently of the type of input data. They have recently been extended to recurrent neural networks [66], graph neural networks [67], transformers [68], and state space models [69], which represent the state of the art for large language models and other models of structured data. Thus, our analysis could be extended to analyze other instances of unsupervised learning, such as anomaly detection in time series or the representations learned by large language models (e.g. [70, 71]).

Overall, we believe that the CH effect in unsupervised learning, and the uncontrolled risks associated with it, is a question of general importance, and that Explainable AI and its recent developments provide an effective way to tackle it.

Methods

This section first introduces the unsupervised ML models studied in this work and the datasets on which they are applied. It then presents the layer-wise relevance propagation (LRP) method for explaining predictions, its BiLRP extension for explaining similarity, and the technique of ‘virtual layers’ for generating joint pixel-frequency explanations.

ML Models and Data for Representation Learning

Representation learning experiments were performed on the SimCLR [12, 38], CLIP[13], BarlowTwins [39] and PubMedCLIP [36] models. All include a version based on

the ResNet50 architecture [72] and come with pre-trained weights. SimCLR augments the input images with resized crops, color jitter, and Gaussian blur to create two different views of the same image. These views are then used to create positive and negative pairs, where the positive pairs represent the same image from two different perspectives, and the negative pairs are created by pairing different images. The contrastive loss objective maximizes the similarity between the representations of the positive pairs while minimizing the similarity between the representations of the negative pairs. Barlow Twins is similar to SimCLR in that it also generates augmented views of the input image through random resized crops and color augmentation, and maximizes their cosine similarity in representation space. However, it differs from SimCLR in the exact mechanisms used to prevent representation collapse. In our experiments, we use the weights from the vissl³ library. CLIP (and its derivative PubMedCLIP) learns representations by using a large collection of image-text pairs from the Internet. Images are given to an image encoder, and the corresponding texts are given to a text encoder. The similarity of the two resulting embeddings is then maximized with a contrastive loss. In our experiments, we use the ResNet-50 weights from OpenAI⁴ for CLIP. PubMedCLIP⁵ is based on a pre-trained CLIP model fine-tuned on the ROCO dataset [73], a collection of radiology and image caption pairs. For all representation learning experiments, the *supervised baselines* share the same architecture as their unsupervised counterparts, but are trained in a purely supervised fashion using backpropagation.

The analysis and training of these models were performed on different datasets. The ImageNet experiments were performed on two ImageNet subsets. First, the ‘truck’ subset consisting of the 8 classes sharing the WordNetID ‘truck’ (minivan, moving van, police van, fire engine, garbage truck, pickup, tow truck and trailer truck). Then the ‘fish’ subset consisting of the 16 classes sharing the WordNetID ‘fish’ (tench, barracouta, coho, sturgeon, gar, stingray, great white shark, hammerhead, tiger shark, puffer, electric ray, goldfish, eel, anemone fish, rock beauty and lionfish). For the X-ray experiments, we combined the NIH ChestX-ray8 (CXR8) dataset⁶ and the GitHub-hosted ‘COVID-19 image data collection’⁷. The NIH dataset contributed 2597 negative images, while the GitHub dataset contained 342 COVID-positive and 193 negative images. All images were resized to 224x224 pixels and center-cropped. We split the patients 80:20 into training and test sets based on unique patient IDs. This resulted in 272 positive and 168 negative images in

the training set from the GitHub dataset. To approximate an i.i.d. distribution in the training set, we added 2552 negative images from the NIH dataset, resulting in a total of 2992 training images (272 positive, 2720 negative). The test set consisted of 70 positive and 70 negative images, with 45 negative images from the NIH dataset and 25 from the GitHub dataset. This resulted in 2552 NIH images and 440 GitHub images in the training set, and 45 NIH images and 95 GitHub images in the test set.

ML Models and Data for Anomaly Detection

The *D2Neighbors* model used in our experiments is an instance of the family of distance-based anomaly detectors, which encompasses a variety of methods from the literature [2, 47–49, 74, 75]. The D2Neighbors model computes anomaly scores as $o(\mathbf{x}) = \mathbb{M}_j^\gamma \{ \|\mathbf{x} - \mathbf{u}_j\|_p^p \}$ where \mathbf{x} is the input, $(\mathbf{u}_j)_{j=1}^N$ are the training data, and \mathbb{M}^γ is a generalized f -mean, with function $f(t) = \exp(-\gamma t)$. The function can be interpreted as a soft minimum over distances to data points, i.e. a distance to the nearest neighbors. In our experiments, the data received as input are RGB images of size 224×224 with pixel values encoded between -1 and 1 , down-sized from their original high resolution using OpenCV’s fast nearest neighbor interpolation. We set γ so that the average perplexity [76] equals 25% of the training set size for each model.

We also consider the PatchCore [45] anomaly detection model, which uses mid-level patch features from a fixed pre-trained network. It constructs a memory bank of these features from nominal example images during training. Anomaly scores for test images are computed by finding the maximum distance between each test patch feature and its nearest neighbor in the memory bank. Distances are computed between patch features $\phi_p(\mathbf{x})$ and a memory bank of location independent prototypes $(\mathbf{u}_j)_{j=1}^N$. The overall outlier scoring function of PatchCore can be written as $o(\mathbf{x}) = \max_k \min_j \|\phi_k(\mathbf{x}) - \mathbf{u}_j\|$. The function ϕ_k is the feature representation aggregated from two consecutive layers at spatial patch location k , extracted from a pre-trained WideResNet50. The features from consecutive layers are aggregated by rescaling and concatenating the feature maps. The difference between our reported F1 scores and those in [45] is mainly due to the method used to resize the images. We used the authors’ reference implementation⁸ as the basis for our experiments.

All of the above models were trained on the MVTec dataset. The MVTec dataset consists of 15 image categories (‘bottle’, ‘cable’, ‘capsule’, ‘carpet’, ‘grid’, ‘hazelnut’, ‘leather’, ‘metal nut’, ‘pill’, ‘screw’, ‘tile’, ‘toothbrush’, ‘transistor’, ‘wood’ and ‘zipper’) of industrial objects and textures,

³ <https://vissl.ai/>

⁴ <https://github.com/openai/CLIP>

⁵ <https://github.com/sarahESL/PubMedCLIP>

⁶ <https://academictorrents.com/details/e615d3aebce373f1dc8bd9d11064da55bdadede0>

⁷ <https://github.com/ieee8023/covid-chestxray-dataset>

⁸ <https://github.com/amazon-science/patchcore-inspection>

with good and defective instances for each category. For the experiments based on D2Neighbors, we simulated different data preprocessing conditions before and after deployment by changing the way images are resized from their original high resolution to 224×224 pixels. We first use a resizing algorithm found in OpenCV 4.9.0 [77] based on nearest neighbor interpolation. We then simulate post-deployment conditions using an improved resizing method, specifically a bilinear interpolation implemented in Pillow 10.3.0 and used by default in torchvision 0.17.2 [78]. This improved resizing method includes antialiasing, which has the effect of smoothing the transitions between adjacent pixels of the resized image.

Explanations for Representation Learning

Our experiments examined dot product similarities in representation space, i.e. $y = \langle \Phi(\mathbf{x}), \Phi(\mathbf{x}') \rangle$, where Φ denotes the function that maps the input features to the representation, typically a deep neural network. To understand similarity scores in terms of input features, we used the BiLRP method [79] which extends the LRP technique [24, 26, 27, 80] for this specific purpose. The conceptual starting point of BiLRP is the observation that a dot product is a bilinear function of its input. BiLRP then proceeds by reverse propagating the terms of the bilinear function to pairs of activations from the layer below and iterating down to the input. Denoting $R_{kk'}$ the contribution of neurons k and k' to the similarity score in some intermediate layer in the network, BiLRP extracts the contributions of pairs of neurons j and j' in the layer below via the propagation rule:

$$R_{jj'} = \sum_{kk'} \frac{z_{jk} z_{j'k'}}{\sum_{jj'} z_{jk} z_{j'k'}} R_{kk'} \quad (1)$$

In practice, this reverse propagation procedure can be implemented equivalently, but more efficiently and easily, by computing a collection of standard LRP explanations (one for each neuron in the representation layer) and recombining them in a multiplicative manner:

$$\text{BiLRP}(y) = \sum_k \text{LRP}(\Phi_k(\mathbf{x})) \otimes \text{LRP}(\Phi_k(\mathbf{x}')) \quad (2)$$

Overall, assuming the input consists of d features, BiLRP produces an explanation of size $d \times d$ which is typically represented as a weighted bipartite graph between the set of features of the two input images. Due to the large number of terms, pixel-to-pixel contributions are aggregated into patch-to-patch contributions, and elements of the BiLRP explanations that are close to zero are omitted in the final explanation rendering. In our experiments, we computed BiLRP explanations using the Zenit⁹ implementation of

⁹ <https://github.com/chr5tphr/zenit>

LRP which handles the ResNet50 architecture, and set Zenit’s LRP parameters to their default values.

Explanations for the D2Neighbors Model

The D2Neighbors model we investigate for anomaly detection is a composition of a distance layer and a soft min-pooling layer. To handle these layers, we use the purposely designed LRP rules of [28, 53]. Propagation in the softmin layer (\mathbb{M}_j^γ) is given by the formula

$$R_j = \frac{f(\|\mathbf{x} - \mathbf{u}_j\|_p^p)}{\sum_j f(\|\mathbf{x} - \mathbf{u}_j\|_p^p)} o(\mathbf{x}) \quad (3)$$

a ‘min-take-most’ redistribution, where f is the same function as in \mathbb{M}_j^γ . Each score R_j can be interpreted as the contribution of the training point \mathbf{u}_j to the anomaly of \mathbf{x} . To further propagate these scores into the pixel frequency domain, we adopt the framework of ‘virtual layers’ [29, 30] and adapt it to the D2Neighbors model. As a frequency basis, we use the discrete cosine transform (DCT) [54], shown in Fig. 4 (right), which we denote by its collection of basis elements $(\mathbf{v}_k)_k$. Since the DCT forms an orthogonal basis, we have the property $\sum_k \mathbf{v}_k \mathbf{v}_k^\top = I$, and multiplication by the identity matrix can be interpreted as a mapping to the frequencies and back. For the special case where $p = 2$, the distance terms in D2Neighbors reduce to the squared Euclidean norm $\|\mathbf{x} - \mathbf{u}_j\|^2$. These terms can be developed to identify pixel-pixel-frequency interactions: $\|\mathbf{x} - \mathbf{u}_j\|^2 = (\mathbf{x} - \mathbf{u}_j)^\top (\sum_k \mathbf{v}_k \mathbf{v}_k^\top) (\mathbf{x} - \mathbf{u}_j) = \sum_k \sum_{ii'} [\mathbf{x} - \mathbf{u}_j]_i [\mathbf{x} - \mathbf{u}_j]_{i'} [\mathbf{v}_k]_i [\mathbf{v}_k]_{i'}$. From there, one can construct an LRP rule that propagates the instance-wise relevance R_j to the pixel-frequency features:

$$R_{ii'k} = \sum_j \frac{[\mathbf{x} - \mathbf{u}_j]_i [\mathbf{x} - \mathbf{u}_j]_{i'} [\mathbf{v}_k]_i [\mathbf{v}_k]_{i'}}{\epsilon + \|\mathbf{x} - \mathbf{u}_j\|^2} R_j, \quad (4)$$

where the variable ϵ is a small positive term that handles the case where \mathbf{x} and \mathbf{u}_j overlap. A reduction of this propagation rule can be obtained by marginalizing over interacting pixels ($R_{ik} = \sum_{i'} R_{ii'k}$). Further reductions can be obtained by marginalizing over pixels ($R_k = \sum_i R_{ik}$) or frequencies ($R_i = \sum_k R_{ik}$). These reductions are used to generate the heatmaps in Fig. 5.

Data Availability

All data used in this paper, in particular, NIH’s CXR8 [33], GitHub-COVID [34], ImageNet [40], and MVTec-AD [81] are publicly available.

Code Availability

Full code for reproduction of our results is available at <https://git.tu-berlin.de/jackmcrider/the-clever-hans-effect-in-unsupervised-learning>.

Acknowledgements

This work was partly funded by the German Ministry for Education and Research (under refs 01IS14013A-E, 01GQ1115, 01GQ0850, 01IS18056A, 01IS18025A and 01IS18037A), the German Research Foundation (DFG) as Math+: Berlin Mathematics Research Center (EXC 2046/1, project-ID: 390685689) and the DeSBi Research Unit (KI-FOR 5363, project ID: 459422098), and DFG KI-FOR 5363. Furthermore, KRM was partly supported by the Institute of Information & Communications Technology Planning & Evaluation (IITP) grants funded by the Korea government (MSIT) (No. 2019-0-00079, Artificial Intelligence Graduate School Program, Korea University and No. 2022-0-00984, Development of Artificial Intelligence Technology for Personalized Plug-and-Play Explanation and Verification of Explanation). We thank Stefan Ganscha for the valuable comments on the manuscript. Correspondence to KRM and GM.

References

- [1] T. B. Brown *et al.*, “Language models are few-shot learners,” in *NeurIPS*, 2020.
- [2] L. Ruff *et al.*, “A unifying review of deep and shallow anomaly detection,” *Proc. IEEE*, vol. 109, no. 5, pp. 756–795, 2021.
- [3] R. Krishnan, P. Rajpurkar, and E. J. Topol, “Self-supervised learning in medicine and healthcare,” *Nature Biomedical Engineering*, vol. 6, no. 12, pp. 1346–1352, 2022.
- [4] A. Li *et al.*, “Unsupervised analysis of transcriptomic profiles reveals six glioma subtypes,” *Cancer Research*, vol. 69, no. 5, pp. 2091–2099, 2009.
- [5] L. Jiang, Y. Xiao, Y. Ding, J. Tang, and F. Guo, “Discovering cancer subtypes via an accurate fusion strategy on multiple profile data,” *Frontiers in Genetics*, vol. 10, 2019.
- [6] O. Eberle, J. Büttner, H. El-Hajj, G. Montavon, K.-R. Müller, and M. Valleriani, “Insightful analysis of historical sources at scales beyond human capabilities using unsupervised machine learning and XAI,” *arXiv 2310.09091*, 2023.
- [7] L. Rettig, M. Khayati, P. Cudré-Mauroux, and M. Piórkowski, “Online anomaly detection over big data streams,” in *Applied Data Science*, Springer, 2019, pp. 289–312.
- [8] E. Eskin, A. Arnold, M. J. Prerau, L. Portnoy, and S. J. Stolfo, “A geometric framework for unsupervised anomaly detection,” in *Applications of Data Mining in Computer Security*, ser. Advances in Information Security, Springer, 2002, pp. 77–101.
- [9] P. Bergmann, K. Batzner, M. Fauser, D. Sattlegger, and C. Steger, “The mvtec anomaly detection dataset: A comprehensive real-world dataset for unsupervised anomaly detection,” *Int. J. Comput. Vis.*, vol. 129, no. 4, pp. 1038–1059, 2021.
- [10] J. Zipfel, F. Verwornner, M. Fischer, U. Wieland, M. Kraus, and P. Zschech, “Anomaly detection for industrial quality assurance: A comparative evaluation of unsupervised deep learning models,” *Comput. Ind. Eng.*, vol. 177, p. 109045, 2023.
- [11] R. Bommasani *et al.*, “On the opportunities and risks of foundation models,” *arXiv 2108.07258*, 2021.
- [12] T. Chen, S. Kornblith, K. Swersky, M. Norouzi, and G. E. Hinton, “Big self-supervised models are strong semi-supervised learners,” in *NeurIPS*, 2020.
- [13] A. Radford *et al.*, “Learning transferable visual models from natural language supervision,” in *ICML*, ser. Proceedings of Machine Learning Research, vol. 139, 2021, pp. 8748–8763.
- [14] M. Moor *et al.*, “Foundation models for generalist medical artificial intelligence,” *Nature*, vol. 616, no. 7956, pp. 259–265, Apr. 2023, issn: 1476-4687.
- [15] J. Dippel *et al.*, “RudolfV: A foundation model by pathologists for pathologists,” *arXiv 2401.04079*, 2024.
- [16] S. Lapuschkin, S. Wäldchen, A. Binder, G. Montavon, W. Samek, and K.-R. Müller, “Unmasking Clever Hans predictors and assessing what machines really learn,” *Nature Communications*, vol. 10, no. 1, p. 1096, 2019.
- [17] R. Geirhos *et al.*, “Shortcut learning in deep neural networks,” *Nat. Mach. Intell.*, vol. 2, no. 11, pp. 665–673, 2020.
- [18] C. J. Anders, L. Weber, D. Neumann, W. Samek, K.-R. Müller, and S. Lapuschkin, “Finding and removing Clever Hans: Using explanation methods to debug and improve deep models,” *Inf. Fusion*, vol. 77, pp. 261–295, 2022.
- [19] L. Linhardt, K.-R. Müller, and G. Montavon, “Preemptively pruning Clever-Hans strategies in deep neural networks,” *Information Fusion*, vol. 103, p. 102094, 2024.
- [20] J. K. Winkler *et al.*, “Association between surgical skin markings in dermoscopic images and diagnostic performance of a deep learning convolutional neural network for melanoma recognition,” *JAMA Dermatology*, vol. 155, no. 10, pp. 1135–1141, 2019.
- [21] G. Montavon, W. Samek, and K.-R. Müller, “Methods for interpreting and understanding deep neural networks,” *Digital signal processing*, vol. 73, pp. 1–15, 2018.
- [22] D. Gunning, M. Stefik, J. Choi, T. Miller, S. Stumpf, and G.-Z. Yang, “XAI-explainable artificial intelligence,” *Science robotics*, vol. 4, no. 37, eaay7120, 2019.
- [23] A. B. Arrieta *et al.*, “Explainable artificial intelligence (XAI): concepts, taxonomies, opportunities and challenges toward responsible AI,” *Inf. Fusion*, vol. 58, pp. 82–115, 2020.

- [24] W. Samek, G. Montavon, S. Lapuschkin, C. J. Anders, and K.-R. Müller, “Explaining deep neural networks and beyond: A review of methods and applications,” *Proceedings of the IEEE*, vol. 109, no. 3, pp. 247–278, 2021.
- [25] F. Klauschen *et al.*, “Toward explainable artificial intelligence for precision pathology,” *Annual Review of Pathology: Mechanisms of Disease*, vol. 19, pp. 541–570, 2024.
- [26] S. Bach, A. Binder, G. Montavon, F. Klauschen, K.-R. Müller, and W. Samek, “On pixel-wise explanations for non-linear classifier decisions by layer-wise relevance propagation,” *PLOS ONE*, vol. 10, no. 7, e0130140, Jul. 2015.
- [27] G. Montavon, A. Binder, S. Lapuschkin, W. Samek, and K.-R. Müller, “Layer-wise relevance propagation: An overview,” in *Explainable AI*, ser. Lecture Notes in Computer Science, vol. 11700, Springer, 2019, pp. 193–209.
- [28] J. Kauffmann, K.-R. Müller, and G. Montavon, “Towards explaining anomalies: A deep Taylor decomposition of one-class models,” *Pattern Recognition*, vol. 101, p. 107 198, 2020.
- [29] J. Vielhaben, S. Lapuschkin, G. Montavon, and W. Samek, “Explainable AI for time series via virtual inspection layers,” *Pattern Recognition*, vol. 150, p. 110 309, 2024.
- [30] P. Chormai, J. Herrmann, K.-R. Müller, and G. Montavon, “Disentangled explanations of neural network predictions by finding relevant subspaces,” *IEEE Trans. Pattern Anal. Mach. Intell.*, pp. 1–18, 2024. DOI: 10.1109/TPAMI.2024.3388275.
- [31] L. Wang, Z. Q. Lin, and A. Wong, “COVID-Net: A tailored deep convolutional neural network design for detection of COVID-19 cases from chest X-ray images,” *Scientific Reports*, vol. 10, no. 1, 2020.
- [32] A. J. DeGrave, J. D. Janizek, and S.-I. Lee, “Ai for radiographic covid-19 detection selects shortcuts over signal,” *Nature Machine Intelligence*, vol. 3, no. 7, pp. 610–619, May 2021.
- [33] X. Wang, Y. Peng, L. Lu, Z. Lu, M. Bagheri, and R. M. Summers, “Chestx-ray8: Hospital-scale chest x-ray database and benchmarks on weakly-supervised classification and localization of common thorax diseases,” in *2017 IEEE Conference on Computer Vision and Pattern Recognition (CVPR)*, IEEE, 2017.
- [34] J. P. Cohen, P. Morrison, L. Dao, K. Roth, T. Q. Duong, and M. Ghassemi, “COVID-19 image data collection: Prospective predictions are the future,” *arXiv 2006.11988*, 2020.
- [35] S. Azizi *et al.*, “Big self-supervised models advance medical image classification,” in *ICCV*, IEEE, 2021, pp. 3458–3468.
- [36] S. Eslami, C. Meinel, and G. de Melo, “PubMedCLIP: How much does CLIP benefit visual question answering in the medical domain?” In *EACL (Findings)*, Association for Computational Linguistics, 2023, pp. 1151–1163.
- [37] S.-C. Huang, A. Pareek, M. Jensen, M. P. Lungren, S. Yeung, and A. S. Chaudhari, “Self-supervised learning for medical image classification: A systematic review and implementation guidelines,” *npj Digital Medicine*, vol. 6, no. 1, Apr. 2023, ISSN: 2398-6352.
- [38] T. Chen, S. Kornblith, M. Norouzi, and G. E. Hinton, “A simple framework for contrastive learning of visual representations,” in *ICML*, ser. Proceedings of Machine Learning Research, vol. 119, 2020, pp. 1597–1607.
- [39] J. Zbontar, L. Jing, I. Misra, Y. LeCun, and S. Deny, “Barlow twins: Self-supervised learning via redundancy reduction,” in *ICML*, ser. Proceedings of Machine Learning Research, vol. 139, 2021, pp. 12 310–12 320.
- [40] J. Deng, W. Dong, R. Socher, L. Li, K. Li, and L. Fei-Fei, “Imagenet: A large-scale hierarchical image database,” in *CVPR*, IEEE Computer Society, 2009, pp. 248–255.
- [41] T. Chen, C. Luo, and L. Li, “Intriguing properties of contrastive losses,” in *NeurIPS*, 2021, pp. 11 834–11 845.
- [42] J. Robinson, L. Sun, K. Yu, K. Batmanghelich, S. Jegelka, and S. Sra, “Can contrastive learning avoid shortcut solutions?” In *NeurIPS*, 2021, pp. 4974–4986.
- [43] J. Dippel, S. Vogler, and J. Höhne, *Towards fine-grained visual representations by combining contrastive learning with image reconstruction and attention-weighted pooling*, ICML Workshop: Self-Supervised Learning for Reasoning and Perception, 2021.
- [44] T. Li *et al.*, “Addressing feature suppression in unsupervised visual representations,” in *WACV*, IEEE, 2023, pp. 1411–1420.
- [45] K. Roth, L. Pemula, J. Zepeda, B. Schölkopf, T. Brox, and P. V. Gehler, “Towards total recall in industrial anomaly detection,” in *IEEE/CVF Conference on Computer Vision and Pattern Recognition*, IEEE, 2022, pp. 14 298–14 308.
- [46] K. Batzner, L. Heckler, and R. König, “Efficientad: Accurate visual anomaly detection at millisecond-level latencies,” in *WACV*, IEEE, 2024, pp. 127–137.
- [47] S. Harmeling, G. Dornhege, D. Tax, F. Meinecke, and K.-R. Müller, “From outliers to prototypes: Ordering data,” *Neurocomputing*, vol. 69, no. 13, pp. 1608–1618, 2006.
- [48] C. C. Aggarwal, *Outlier Analysis*. Springer, 2013.
- [49] V. Chandola, A. Banerjee, and V. Kumar, “Anomaly detection: A survey,” *ACM Comput. Surv.*, vol. 41, no. 3, 15:1–15:58, 2009.
- [50] E. Parzen, “On estimation of a probability density function and mode,” *The Annals of Mathematical Statistics*, vol. 33, no. 3, pp. 1065–1076, Sep. 1962.
- [51] J. Kim and C. D. Scott, “Robust kernel density estimation,” *J. Mach. Learn. Res.*, vol. 13, pp. 2529–2565, 2012.
- [52] B. Schölkopf, J. C. Platt, J. Shawe-Taylor, A. J. Smola, and R. C. Williamson, “Estimating the support of a high-dimensional distribution,” *Neural Comput.*, vol. 13, no. 7, pp. 1443–1471, 2001.

- [53] G. Montavon, J. Kauffmann, W. Samek, and K.-R. Müller, “Explaining the predictions of unsupervised learning models,” in *xxAI - Beyond Explainable AI*, ser. Lecture Notes in Artificial Intelligence, vol. 13200, 2022, pp. 117–138.
- [54] Y. Yu, J. Qian, and Q. Wu, “Visual saliency via multi-scale analysis in frequency domain and its applications to ship detection in optical satellite images,” *Frontiers in Neurobotics*, vol. 15, 2022.
- [55] G. Parmar, R. Zhang, and J. Zhu, “On aliased resizing and surprising subtleties in GAN evaluation,” in *CVPR*, IEEE, 2022, pp. 11 400–11 410.
- [56] M. Sugiyama, M. Krauledat, and K.-R. Müller, “Covariate shift adaptation by importance weighted cross validation,” *Journal of Machine Learning Research*, vol. 8, no. 5, pp. 985–1005, 2007.
- [57] M. Sugiyama and M. Kawanabe, *Machine learning in non-stationary environments: Introduction to covariate shift adaptation*. MIT press, 2012.
- [58] Y. Iwasawa and Y. Matsuo, “Test-time classifier adjustment module for model-agnostic domain generalization,” in *NeurIPS*, 2021, pp. 2427–2440.
- [59] C. Esposito, G. A. Landrum, N. Schneider, N. Stiefl, and S. Riniker, “Ghost: Adjusting the decision threshold to handle imbalanced data in machine learning,” *Journal of Chemical Information and Modeling*, vol. 61, no. 6, pp. 2623–2640, 2021.
- [60] P. Kirichenko, P. Izmailov, and A. G. Wilson, “Last layer re-training is sufficient for robustness to spurious correlations,” in *ICLR*, OpenReview.net, 2023.
- [61] T. Niven and H. Kao, “Probing neural network comprehension of natural language arguments,” in *ACL (1)*, Association for Computational Linguistics, 2019, pp. 4658–4664.
- [62] B. Heinzerling, “NLP’s Clever Hans moment has arrived,” *The Journal of Cognitive Science*, vol. 21, pp. 161–170, 2020.
- [63] M. L. Braun, J. M. Buhmann, and K.-R. Müller, “On relevant dimensions in kernel feature spaces,” *J. Mach. Learn. Res.*, vol. 9, pp. 1875–1908, 2008.
- [64] R. Basri, M. Galun, A. Geifman, D. W. Jacobs, Y. Kasten, and S. Kritchman, “Frequency bias in neural networks for input of non-uniform density,” in *ICML*, ser. Proceedings of Machine Learning Research, vol. 119, 2020, pp. 685–694.
- [65] S. Fridovich-Keil, R. G. Lopes, and R. Roelofs, “Spectral bias in practice: The role of function frequency in generalization,” in *NeurIPS*, 2022.
- [66] L. Arras *et al.*, “Explaining and interpreting lstms,” in *Explainable AI*, ser. Lecture Notes in Computer Science, vol. 11700, Springer, 2019, pp. 211–238.
- [67] T. Schnake *et al.*, “Higher-order explanations of graph neural networks via relevant walks,” *IEEE Trans. Pattern Anal. Mach. Intell.*, vol. 44, no. 11, pp. 7581–7596, 2022.
- [68] A. Ali, T. Schnake, O. Eberle, G. Montavon, K. Müller, and L. Wolf, “XAI for transformers: Better explanations through conservative propagation,” in *ICML*, ser. Proceedings of Machine Learning Research, vol. 162, 2022, pp. 435–451.
- [69] F. R. Jafari, G. Montavon, K.-R. Müller, and O. Eberle, “MambaLRP: Explaining selective state space sequence models,” *arXiv 2406.07592*, 2024.
- [70] M. Munir, S. A. Siddiqui, A. Dengel, and S. Ahmed, “Deepant: A deep learning approach for unsupervised anomaly detection in time series,” *IEEE Access*, vol. 7, pp. 1991–2005, 2019.
- [71] J. Devlin, M. Chang, K. Lee, and K. Toutanova, “BERT: pre-training of deep bidirectional transformers for language understanding,” in *NAACL-HLT (1)*, Association for Computational Linguistics, 2019, pp. 4171–4186.
- [72] K. He, X. Zhang, S. Ren, and J. Sun, “Deep residual learning for image recognition,” in *Proceedings of the IEEE conference on computer vision and pattern recognition*, 2016, pp. 770–778.
- [73] O. Pelka, S. Koitka, J. Rückert, F. Nensa, and C. M. Friedrich, “Radiology objects in context (ROCO): A multi-modal image dataset,” in *Intravascular Imaging and Computer Assisted Stenting - and - Large-Scale Annotation of Biomedical Data and Expert Label Synthesis*, D. Stoyanov *et al.*, Eds., ser. Lecture Notes in Computer Science, vol. 11043, Springer, 2018, pp. 180–189.
- [74] G. Pang, C. Shen, L. Cao, and A. van den Hengel, “Deep learning for anomaly detection: A review,” *ACM Comput. Surv.*, vol. 54, no. 2, 38:1–38:38, 2022.
- [75] O. Rippel, P. Mertens, and D. Merhof, “Modeling the distribution of normal data in pre-trained deep features for anomaly detection,” in *ICPR*, IEEE, 2020, pp. 6726–6733.
- [76] F. Jelinek, R. L. Mercer, L. R. Bahl, and J. K. Baker, “Perplexity—a measure of the difficulty of speech recognition tasks,” *The Journal of the Acoustical Society of America*, vol. 62, no. S1, S63–S63, Aug. 2005.
- [77] G. Bradski, “The OpenCV Library,” *Dr. Dobb’s Journal of Software Tools*, 2000.
- [78] TorchVision maintainers and contributors, *Torchvision: Pytorch’s computer vision library*, <https://github.com/pytorch/vision>, 2016.
- [79] O. Eberle, J. Büttner, F. Kräutli, K. Müller, M. Valleriani, and G. Montavon, “Building and interpreting deep similarity models,” *IEEE Trans. Pattern Anal. Mach. Intell.*, vol. 44, no. 3, pp. 1149–1161, 2022.
- [80] W. Samek, G. Montavon, A. Vedaldi, L. K. Hansen, and K.-R. Müller, *Explainable AI: interpreting, explaining and visualizing deep learning*. Springer Nature, 2019, vol. 11700.
- [81] P. Bergmann, M. Fauser, D. Sattlegger, and C. Steger, “MVTec AD - A comprehensive real-world dataset for unsupervised anomaly detection,” in *CVPR*, Computer Vision Foundation / IEEE, 2019, pp. 9592–9600.

The Clever Hans Effect in Unsupervised Learning

(SUPPLEMENTARY NOTES)

Jacob Kauffmann, Jonas Dippel, Lukas Ruff, Wojciech Samek,
Klaus-Robert Müller and Grégoire Montavon

1 These supplementary notes provide detailed results and analysis of the experiments conducted
2 in the main paper. They aim to further support the main paper’s claims about the prominence
3 and distinctiveness of the Clever Hans effect in unsupervised learning, and the importance of
4 addressing it in order to achieve unsupervised models that are more robust and reliable for
5 downstream applications.

6 **Supplementary Note A. Additional Results for X-Ray Representations**

7 Recall from the main paper that we analyzed the PubMedCLIP’s foundation model [1], specifically
8 its representation of X-ray data and its use for a downstream COVID-19 detection task. For this
9 purpose, we considered a dataset constructed by merging the NIH CXR8 dataset [2] with the
10 Github-hosted ‘COVID-19 Image Data Collection’ [3], and referred to these two data sources as
11 NIH and Github. The NIH data, collected before the onset of the COVID-19 pandemic, is from a
12 single hospital and is relatively homogeneous. The Github data, collected from multiple sources,
13 is more heterogeneous. In the main paper, we reported strong inhomogeneities in the classification
14 of the data across different subgroups, with the NIH instances being systematically correctly
15 classified as negative and, in contrast, numerous Github negative instances being classified as
16 positive. We attributed this heterogeneity in prediction quality to a spurious reliance on textual
17 or annotation artifacts already latent in the representation of the unsupervised PubMedCLIP
18 model. In this supplementary note, we retrace the emergence of the heterogeneous classification
19 behavior from the representation level up to the classifier by providing further examples and
20 analyses.

21 **Analysis of the Unsupervised Representation**

22 In the main paper, we proposed to look at representation from the perspective of similarity
23 between pairs of instances, and we expressed similarity as dot products in representation space
24 (e.g. [4]):

$$k(x, x') = \Phi(x)^\top \Phi(x') \quad (1)$$

25 The function Φ represents PubMedCLIP’s mapping from raw pixel values to its representation.
26 Fig. 1 (left) shows the output of our BiLRP analysis, highlighting pairs of features responsible
27 for the high measured dot-product similarity. Our analysis systematically highlights that the
28 predicted similarity is supported by spurious annotations on the X-ray images instead of the
29 underlying pathology, a clear case of a Clever Hans effect. In other words, the PubMedCLIP
30 representation supports similarity predictions that are right for the wrong reasons. Furthermore,
31 the type and location of these artifacts used by PubMedCLIP vary across the subgroups of the
32 dataset, with the artifacts in the NIH subgroup being much more homogeneous than those in
33 the Github subgroup.

34 The reliance of the PubMedCLIP model on features that code for dataset-specific annotation
35 artifacts rather than the underlying pathology can also be demonstrated by performing a t-SNE
36 analysis [5] of its representation. We color code each data point in the t-SNE visualization
37 according to its provenance (NIH or Github). The visualization is shown in Fig. 1 (right). It

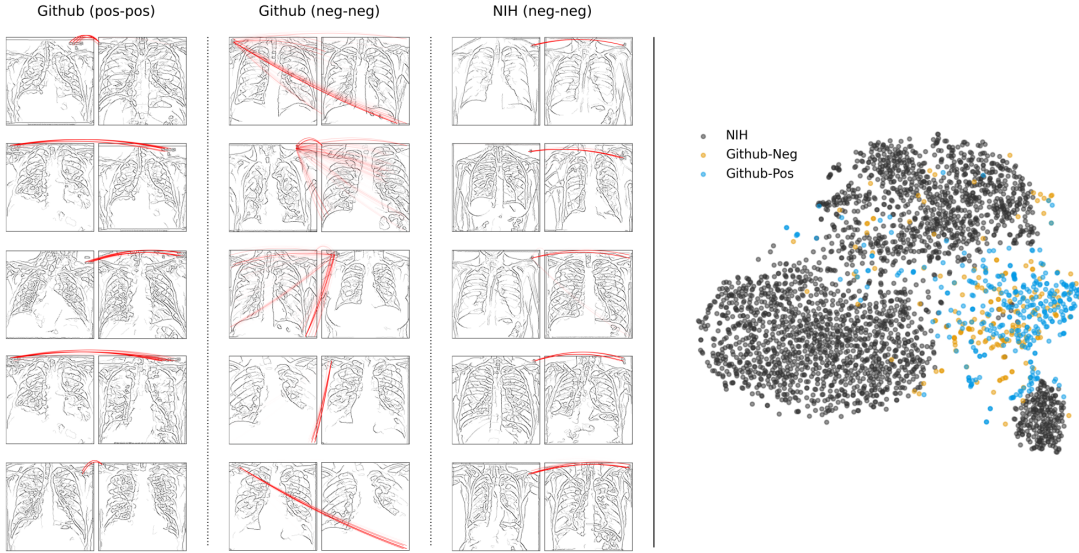


Figure 1: Left: BiLRP explanations of PubMedCLIP’s dot-product similarity scores for X-ray image pairs belonging to the same class and data subset. Red curves indicate pairs of features of the two images that support the similarity prediction. Right: T-SNE analysis of PubMedCLIP’s representation of X-ray data. Colors indicate the data source (NIH CXR8 [2] or Github-Covid [3]) and the ground truth label (COVID-positive or COVID-negative).

38 reveals a cluster structure in the data representation, where the clusters are more predictive
 39 of data provenance than COVID negativity/positivity. While the COVID-positives cluster at
 40 rather specific locations in the t-SNE space, they overlap significantly with the COVID-negatives
 41 from the Github dataset. Finally, it should be noted that while color-coded T-SNE analysis (and
 42 other correlational analyses for that matter) can establish the prominence of an already identified
 43 artifact or source of heterogeneity in the representation, our Explainable AI analysis does not
 44 require prior knowledge of the data artifact and can instead assist a human in identifying it.

45 Analysis of the Downstream Classifier

46 We now examine the transmission of the CH effect from the representation learning model
 47 to the downstream classifier. We recall from the main paper that we built a linear readout
 48 $f(x) = w^\top \Phi(x) + \theta$ on top of the PubMedCLIP representation. Specifically, we have trained a
 49 linear SVM classifier on the COVID detection task, where $f(x) < 0$ represents COVID negatives
 50 and $f(x) > 0$ represents COVID positives. Note that the same SVM classifier can also be
 51 formulated in terms of dot-product similarities:

$$f(x) = \sum_{i=1}^N \alpha_i k(x, x_i) + \theta \quad (2)$$

52 The predictions of the SVM can thus be seen as a combination of dot-product similarities of
 53 the type we analyzed above. After training the SVM model and selecting the hyperparameters
 54 using hold-out validation, we found that $C = 0.01$ and a class weighting scheme adjusted to
 55 balance the class representation yielded the best performance. We examine the SVM prediction
 56 performance over the different data subgroups. The results are shown in Table 1. We observe a
 57 strong inhomogeneity of performance between different data sources.

58 To further shed light on the instability in the SVM’s decision strategy, we use the LRP
 59 explanation technique [6, 7]. LRP allows us to identify, for each predicted instance, the extent
 60 to which each input pixel contributed to the prediction. The results are shown in Fig. 2 for a
 61 selection of correctly classified instances from each data subgroup. Similar to the BiLRP analysis

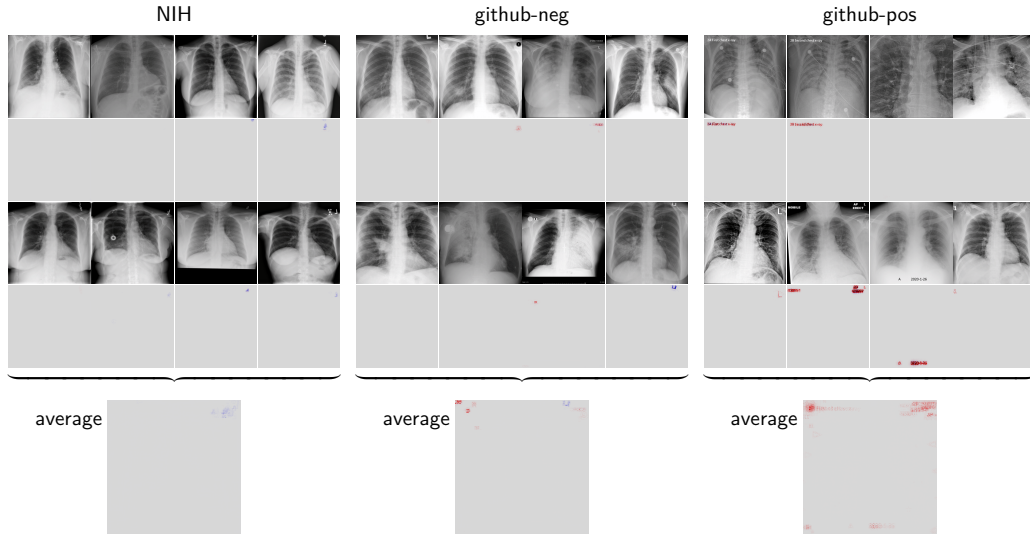


Figure 2: LRP explanations for COVID-19 detection. Top: Exemplary chest X-ray images from each data subgroup along with explanations showing pixel-wise evidence for/against COVID-19 as perceived by the model. Bottom: Explanations averaged over the entire subgroup. Red color indicates regions contributing evidence for COVID-19, while blue color indicates evidence against COVID-19.

62 above, our LRP analysis of the SVM classifier reveals a strong reliance of the model on spurious
 63 annotations, with COVID-positive instances again being the ones most strongly supported by
 64 artifacts. The LRP analysis also reveals that COVID-negative predictions are supported by
 65 annotation artifacts. The latter, however, differ from the positive ones in that they systematically
 66 occur in the upper right corner of the input image. This Clever Hans-like prediction strategy,
 67 combined with the fact that the artifacts differ across datasets, explains the unstable prediction
 68 performance of the classifier. In particular, the high false positive rate (FPR) of the SVM on
 69 the Github data can be explained by the fact that the artifacts of the Github negatives do not
 70 coincide with the artifacts of the NIH negatives, with the latter constituting the majority of the
 71 negative instances. As a result, Github negatives fail to be drawn to the negative class and often
 72 end up being misclassified as positives. In summary, our analysis of the downstream classifier
 73 further verifies and scrutinizes the inheritance of the CH effect from the unsupervised model to
 74 the supervised model and its consequences in terms of prediction performance.

75 Supplementary Note B. Additional Results for Generic Image Models

76 In the main paper, we also experimented with generic image models trained with different
 77 unsupervised representation learning algorithms, specifically *SimCLR* [8, 9], BarlowTwins [10]
 78 and *CLIP* [11], the details of which can be found in the methods section of the main paper. We
 79 extend on these experiments by providing further analysis of the learned representations and the
 80 downstream classifiers built on top of them.

	original	github	NIH
Accuracy	88.6	75.2	100.0
False positive rate (FPR)	14%	40%	0%

Table 1: Analysis of a linear SVM built on the PubMedCLIP’s unsupervised foundation model and trained on the COVID classification task. Accuracy and false positive rates are reported for the original data (aggregation of github and NIH sources), and for the individual data sources.

81 **Analysis of the Unsupervised Representations**

82 We first proceed with the BiLRP analysis of each model as well as a purely supervised model (a
 83 standard ResNet50 pre-trained on ImageNet). The results of the analysis are shown in Fig. 3 for
 84 additional image pairs of the class garbage truck and coho, respectively.

85 Recall our findings from the main paper that similarity predictions built on unsupervised
 86 representations are often Clever Hans-like. For example, the similarity between image pairs of
 87 certain fish classes was supported by a human holding the fish in the background (either the
 88 human face for the CLIP model, or the human body for SimCLR and BarlowTwins). Similarly,
 89 for the truck data, the CLIP model was shown to rely heavily on textual logos to express
 90 similarity. Highlighting the heterogeneity of the unsupervised representations, the same textual
 91 logos were suppressed by SimCLR and BarlowTwins, presumably due to their eccentricity in
 92 the image. Here, we complement these results by including a supervised baseline in our analysis
 93 (leftmost example in Fig. 3). We find that the supervised baseline model focuses on task-relevant
 94 features better than unsupervised approaches. However, the supervised baseline also appears to
 95 be overfitted to the task at hand, matching features that belong to the same class, but failing to
 96 disentangle distinct object parts, such as the wheels and the roof of the truck.

97 To further verify the result of the BiLRP analysis, which among other things showed that textual
 98 logos are salient in the CLIP representation, we perform a t-SNE analysis [5] in representation
 99 space. We append to the original truck data an artificial dataset called ‘logo’, consisting of

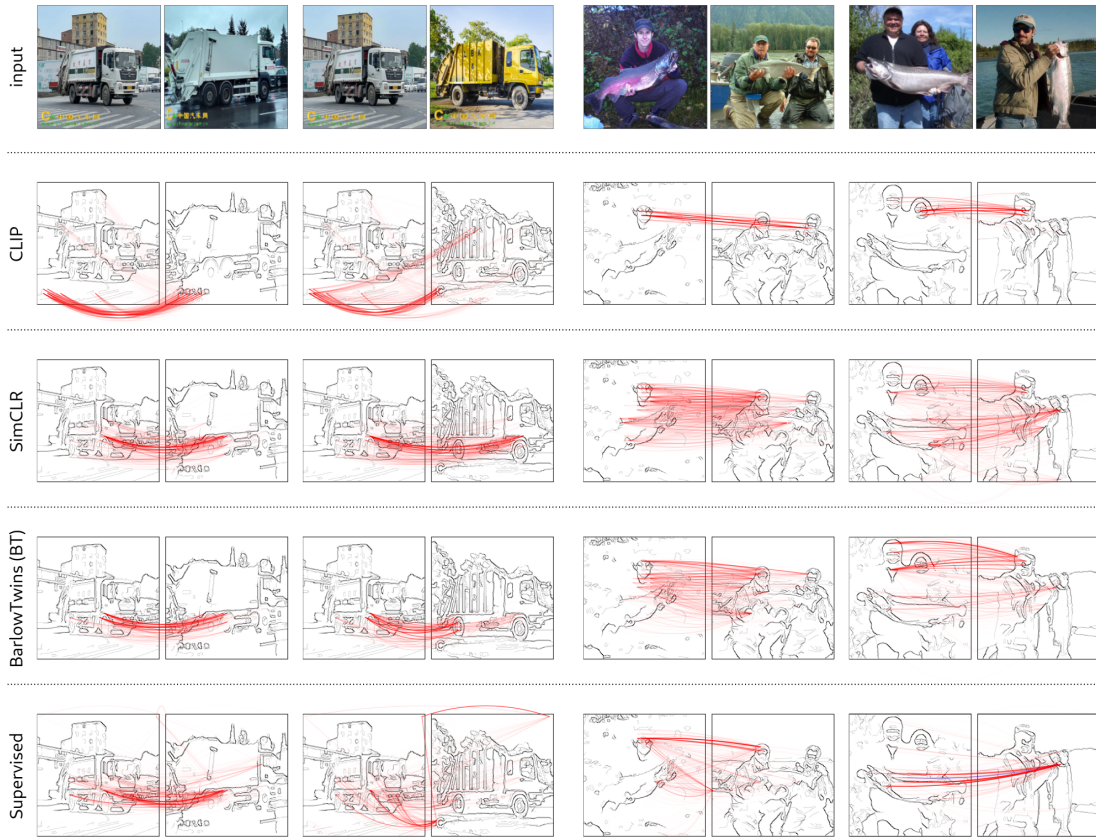


Figure 3: BiLRP explanations of dot product similarities for each representation learning model. The explanations are computed on a selection of ImageNet images from the truck and fish subsets. We observe several Clever Hans effects, such as a reliance on copyright tags in the truck subset and a reliance on humans in the fish subset.

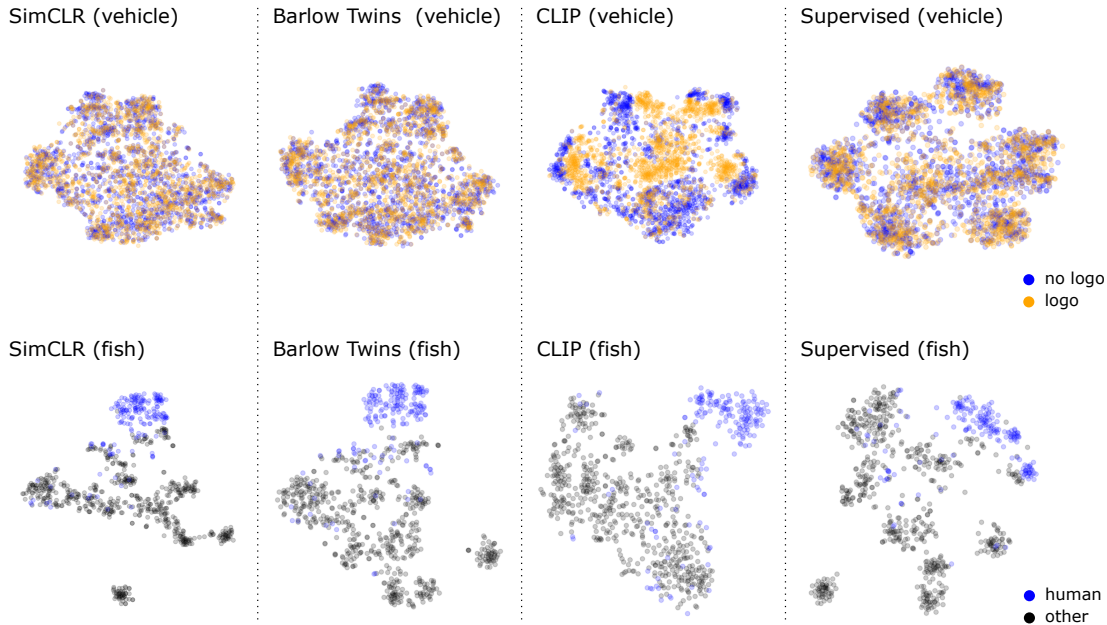


Figure 4: *T-SNE plots of the representations from different models of the truck subset (top) and the fish subset (bottom). For the truck subset, instances are colored according to the presence or absence of a textual logo in the image. For the fish subset, instances are colored according to the presence of a human in the image.*

100 truck data with a textual logo artificially inserted into each image. We then compute a t-SNE
 101 embedding on the augmented data, mapped to the representation of each model. Figure 4 shows
 102 the t-SNE plots for each model’s representation, color-coded by the presence or absence of a
 103 logo. For the CLIP model, the logo is strongly expressed in its representation, as shown by the
 104 yellow and blue dots forming distinct clusters. This suggests that a downstream classifier has an
 105 incentive to use the textual logo as part of its prediction strategy. However, for the SimCLR and
 106 Barlow Twins models, as well as for the supervised baseline, the analysis suggests that the logo
 107 does not play a significant role.

108 We repeat the same t-SNE analysis for the ‘fish’ subset, with the resulting embedding color-
 109 coded according to the presence or absence of a human. We use a Faster R-CNN object detection
 110 model pre-trained on the COCO dataset [12] to classify each image according to whether it
 111 contains a human or not. In each case, we observe high representational similarity of images
 112 containing humans. This suggests that human features are easily accessible when performing the
 113 downstream fish classification task.

114 Analysis of Downstream Classifiers

115 To analyze the transmission of the unsupervised Clever Hans effect from the unsupervised
 116 representation to the downstream supervised models, in the main paper we investigated the
 117 construction of two supervised models on top of each representation (one for fish classification and
 118 one for truck classification). These models are linear-softmax classifiers trained with cross-entropy
 119 loss. We extend the analysis of these classifiers by analyzing their decision strategy using LRP
 120 heatmaps. We use the same LRP procedure that we have used to compute BiLRP explanations,
 121 and we apply the rule LRP-0 [7] in the last readout layer. LRP heatmaps are shown in Fig. 5.
 122 We also report the accuracy scores of each model for each data subset considered in Table 2.
 123 We further elaborate on the structure of the accuracy scores of the problematic data subgroups
 124 (truck images with a logo and fish images with a human) by providing the full confusion matrices
 125 in Fig. 6.

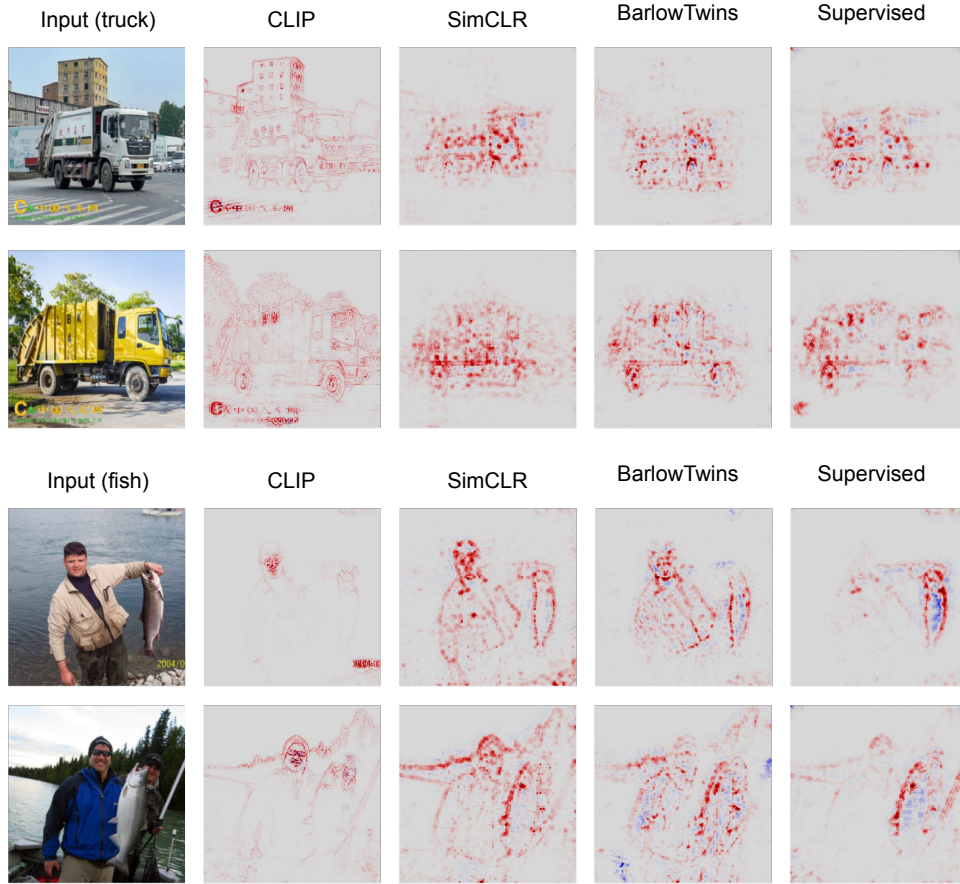


Figure 5: LRP heatmaps for the downstream classification of the fish and truck subsets for different representation learning models. The heatmaps show the pixel-wise contributions to the output of the downstream classifier for the ground truth class. Red color indicates positively contributing pixels and blue color indicates negatively contributing pixels.

126 We start with the truck classification task, where we distinguish between the original data,
 127 consisting of the 50 test images of each truck (400 images in total), and the logo subset, derived
 128 from the original test data by artificially inserting in each image a logo similar to the one found
 129 in the ‘garbage truck’ class. On the original data, we observe that the CLIP model performs best
 130 with an accuracy of 86.6%, followed by 85.7% for the supervised baseline, and sensibly lower
 131 accuracies of 82.9% and 77.7% for the BarlowTwins and SimCLR models, respectively (cf. Table
 132 2, column ‘original’). However, the high accuracy of the CLIP model is partly the result of a
 133 CH strategy based on the detection of a logo in the lower left corner of the image, as shown by
 134 the LRP heatmaps in Fig. 5. In comparison, models built on the BarlowTwins and SimCLR
 135 representations, as well as our supervised baseline, are largely unresponsive to this logo. Notably,
 136 the reliance (or lack thereof) of the supervised model mirrors our BiLRP analysis (cf. Fig. 3),
 137 where only the CLIP model was affected by the logo artifact.

138 Looking at the prediction accuracy on the subgroup of truck images with artificially added
 139 logos (see Table 2, column ‘logo’), the performance of SimCLR, BarlowTwins and our supervised
 140 baseline remains stable compared to the original test data, with a maximum performance drop of
 141 less than 1%. On the other hand, CLIP’s performance drops drastically by almost five percentage

	ImageNet:truck		ImageNet:fish		
	<i>original</i>	logo	<i>original</i>	human	no human
CLIP	85.0	80.5 ↓	86.5	83.8	82.5
+ CH mitigation (1)	85.0	83.8			
+ CH mitigation (2)	84.8	84.0			
+ CH mitigation (5)	85.2	85.0			
+ CH mitigation (10)	85.0	85.0			
+ CH mitigation (20)	81.2	81.2			
SimCLR	74.8	74.5	82.2	78.6	78.4
BarlowTwins	80.2	80.2	83.1	75.6 ↓	81.1
<i>Supervised</i>	83.8	83.2	86.2	84.2	81.9

Table 2: Prediction accuracy obtained by downstream classification models built on the truck and fish subtasks from each representation (including representations enhanced for CH mitigation by removing a given number of spuriously relevant feature maps). Accuracy is reported for the original data, for truck images with an artificially added logo, and for the subgroups of fish images with and without humans.

142 points, making it the worst performer on this subset. The reason for the low accuracy of the
 143 CLIP model is revealed by looking at CLIP’s confusion matrix (cf. Fig. 6). One observes that a
 144 whopping 55.1% of the CLIP model’s errors are misclassifications into the ‘garbage truck’ class,
 145 compared to less than 15% for non-CLIP models.

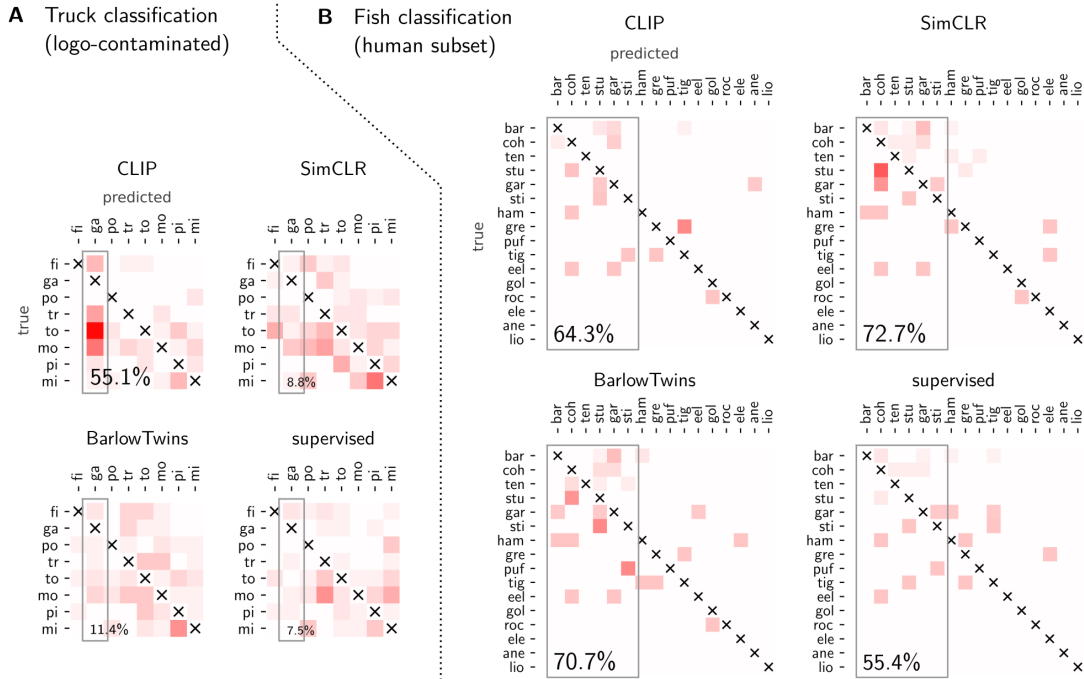


Figure 6: Confusion matrices highlighting the distribution of model errors in terms of true and predicted class. The percentages shown correspond to the proportion of errors falling in the indicated region of the confusion matrix. Abbreviations: [fi]re engine, [ga]rbage truck, [po]lice van, [tr]ailer truck, [to]w truck, [mo]wing van, [pi]ckup, [mi]nivan for the truck classes, and [bar]racouta, [coh]o, [ten]ch, [stu]rgeon, [gar], [sti]ngray, [ham]merhead, [gre]at white shark, [puf]fer, [tig]er shark, [eel], [gol]dfish, [roc]k beauty, [ele]ctric ray, [ane]mone fish, [lio]nfish for the fish classes.

146 We now investigate downstream models that classify the fish ImageNet subset from the different
147 unsupervised representations. All models perform reasonably well on this classification task. The
148 CLIP model ranks first with 86.5%, followed by the supervised model (86.2%), and BarlowTwins
149 and SimCLR with 83.1% and 82.2%, respectively. Figure 5 shows LRP heatmaps explaining
150 the classification by each model of a selection of images from the class ‘coho’. We observe that
151 the CLIP model focuses on the human in the image, specifically the face, rather than the fish.
152 Similarly, the SimCLR and BarlowTwins models also focus on the human, but more specifically
153 on the body. Only the supervised model is reasonably unresponsive to the human and instead
154 clearly focuses on the actual fish to be classified. This shows that the unsupervised learning
155 models studied here all implement a CH strategy. This casts doubt on the generalization of these
156 models and their performance across different subgroups.

157 We investigate the consequence of the identified CH strategies by building a specific subgroup
158 consisting of all fish instances containing humans (e.g. images with a human holding a fish in his
159 hands). This subgroup is built by including only images for which the Faster-R CNN auxiliary
160 model has detected the presence of a human. Since humans are not homogeneously distributed
161 across classes in both training and test data, we rebalance the test data by reweighting all classes
162 containing more than 10 instances in a way that their effective sample size becomes 10. This
163 rebalancing can also be interpreted as a simulation of real-world conditions, removing potentially
164 spurious correlations between fish classes and the presence of a human. On this class-rebalanced
165 subset of data, the accuracy of SimCLR drops below 80%, and BarlowTwins achieves an accuracy
166 of only 75.6%.

167 The decrease in performance for fish classification, as for the truck case, can be understood by
168 looking at the confusion matrices (see Fig. 6). We observe that more than 70% of the errors of
169 the SimCLR and BarlowTwins models correspond to misclassifications as one of the six classes
170 with the highest human prevalence in the original data (‘barracouta’, ‘coho’, ‘tench’, ‘sturgeon’,
171 ‘gar’, ‘stingray’). In contrast, only 55.4% of the errors of the supervised model correspond to
172 this type of misclassification. The reason for the distinct error structure of the SimCLR and
173 BarlowTwins models is that their weak representation of fish features, as shown in the LRP
174 and BiLRP explanations, induces the model to exploit the spurious correlation between human
175 presence and these six classes. As a result, any fish image that contains a human will tend to be
176 predicted, often incorrectly, into one of these classes.

177 **Supplementary Note C. Additional Results for Anomaly Detection**

178 This note complements the unsupervised anomaly detection experiments from the main paper. It
179 provides the Explainable AI analysis and measured performance before and after CH mitigation,
180 for each MVTec category retained in our experiments. Note that our criterion for retaining an
181 MVTec category was that the D2Neighbors model accurately predicts it with F1 scores above
182 0.9 on the original data (cf. Table 3, column *original*).

183 To verify the nature of these accurate anomaly predictions, and in particular to test whether
184 they are based on a valid strategy or instead ‘right for the wrong reasons’, we applied an
185 Explainable AI analysis in the main paper. Here we provide the details of the analysis for
186 the five retained MvTec categories and their corresponding D2Neighbors model. The analysis
187 provides pixel-wise explanations of the predicted anomaly scores. By introducing a Discrete
188 Cosine Transform (DCT) virtual layer, as described in the main paper, the analysis is extended
189 to produce frequency and joint pixel-frequency explanations. Explanations for typical instances
190 of each retained MVTec-AD category are shown in Figure 7.

191 For each MvTec category, the D2Neighbors model responds to a wide range of frequencies,
192 with different frequency bands contributing differently to the decision strategy. In particular,
193 the true anomaly patterns are mostly expressed in the mid-frequency range, while the low and
194 high frequency bands contain artifacts. Especially in the high frequency range, we can see the

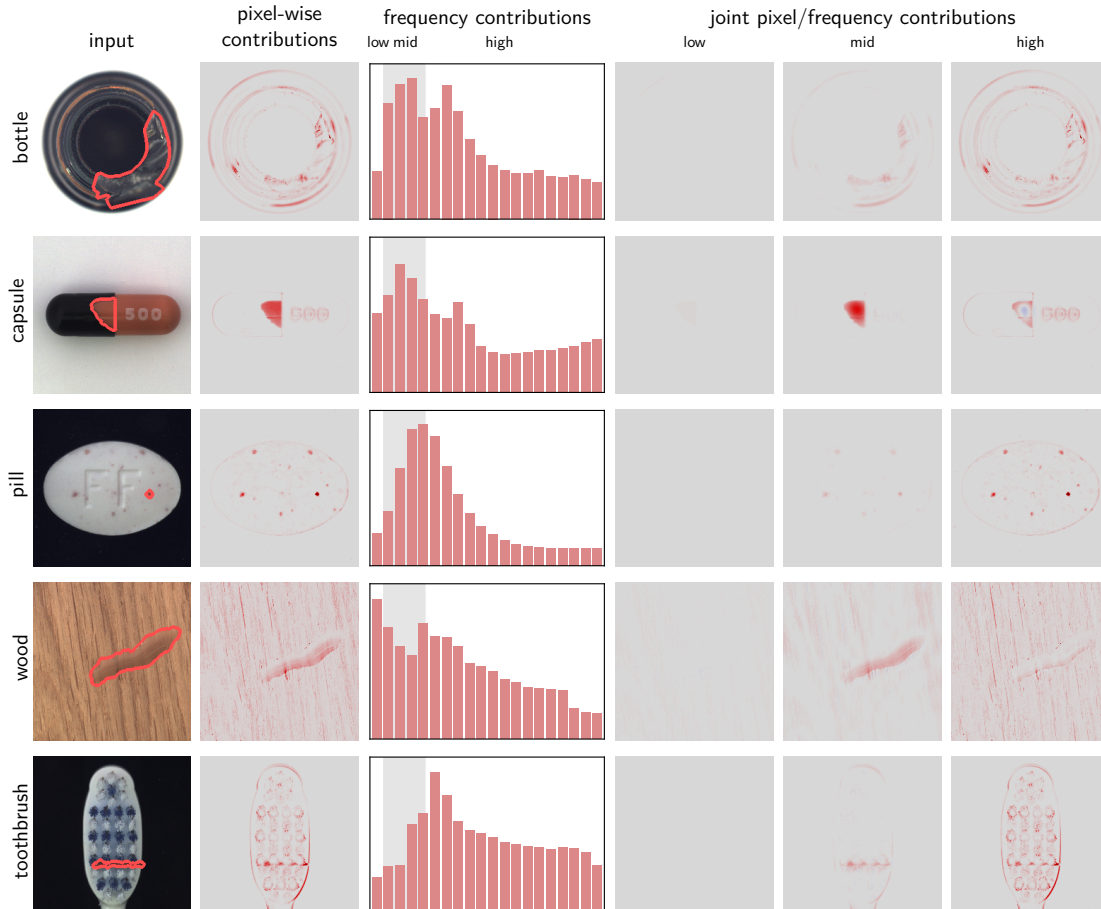


Figure 7: For the retained 5 categories of the MVTEC-AD dataset, we show (from left to right), anomalous input images (with ground truth outlined in red), pixel-wise explanations of the D2Neighbors anomaly predictions, frequency-based explanations, and joint pixel-frequency explanations. For the frequency-based explanations, the x-axis is plotted on a power scale, with bins representing increasingly larger frequency ranges as we move to the high frequencies: (0-2), (3-17), (18-69), (70-188), (189-409), (410-769), (770-1313), (1314-2088), (2089-3142), (3143-4528), (4529-6303), (6304-8525), (8526-11254), (11255-18491), (18492-23132), (23133-28548), (28549-34811), (34812-41995), (41996-50176).

195 model’s response to the border of the bottle, text markings on the capsule, specks on the pill,
 196 wood stripes, or the individual hairs of the toothbrush, all of which are typically not indicative
 197 of a manufacturing defect (the true manufacturing defect is marked with a red outline in the
 198 input image). In other words, our analysis shows that part of D2Neighbors’ anomaly prediction
 199 strategy is of the Clever Hans type.

200 In the main paper, we investigated the consequences of the identified erroneous decision strategy
 201 on the prediction performance under a change in data quality. Specifically, the D2Neighbors
 202 model was trained and validated on MVTEC images resized using a coarse nearest neighbor
 203 interpolation algorithm, and we simulated a post-deployment scenario in which a better bilinear
 204 resizing incorporating antialiasing is being used (details in the methods section of the main
 205 paper). The effect of changing the resizing procedure for one representative image of each MVTEC
 206 category is shown in Figure 8.

207 We observe that the introduction of antialiasing in the resizing procedure strips images of
 208 their high-frequency noise-like components. This suggests that the output of an anomaly model
 209 that is sensitive to high frequencies may be significantly affected, especially if the model’s
 210 exposure to high frequencies is not confined to a particular region of the input image. This

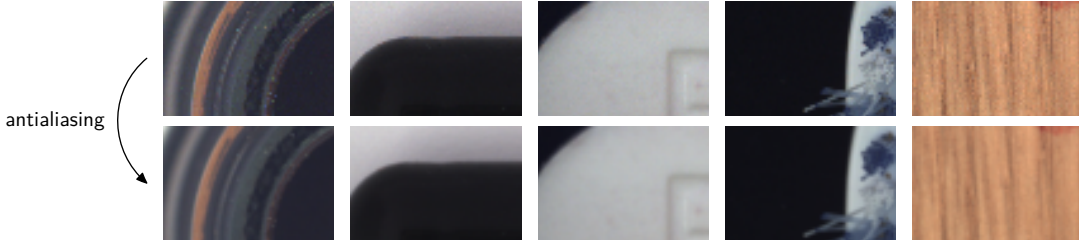


Figure 8: Effect of the resizing procedure on a selection of images from each retained MVTec category. Top: original resizing procedure without antialiasing. Bottom: simulated post-deployment resizing procedure with antialiasing. We can observe that the post-deployment images are sensibly less noisy.

	<i>original</i>	(bot, cap, pil, too, woo)	deployed	(bot, cap, pil, too, woo)
D2Neighbors (ℓ_1)	0.93	(0.89, 0.91, 0.94, 0.97, 0.93)	0.74 ↓	(0.87, 0.45, 0.83, 0.87, 0.71)
+ CH mitigation	0.92	(0.88, 0.91, 0.93, 0.97, 0.94)	0.92 ↑	(0.88, 0.91, 0.93, 0.97, 0.94)
D2Neighbors (ℓ_2)	0.92	(0.90, 0.91, 0.92, 0.93, 0.93)	0.80 ↓	(0.85, 0.73, 0.91, 0.85, 0.67)
+ CH mitigation	0.94	(0.91, 0.92, 0.92, 0.98, 0.95)	0.93 ↑	(0.91, 0.92, 0.92, 0.98, 0.93)
D2Neighbors (ℓ_4)	0.91	(0.92, 0.90, 0.92, 0.90, 0.93)	0.83 ↓	(0.83, 0.88, 0.89, 0.75, 0.78)
+ CH mitigation	0.93	(0.93, 0.90, 0.91, 0.98, 0.93)	0.93 ↑	(0.93, 0.90, 0.91, 0.98, 0.92)
PatchCore	0.92	(0.92, 0.90, 0.92, 0.89, 0.98)	0.85 ↓	(0.91, 0.88, 0.88, 0.64, 0.96)
+ CH mitigation	0.97 ↑	(1.00, 0.96, 0.93, 1.00, 0.95)	0.96 ↑	(1.00, 0.95, 0.93, 0.98, 0.95)

Table 3: F1 scores on the MVTec-AD data per category and averaged. Scores are reported for the simulated original and post-deployment conditions and for a variety of anomaly detection models. Abbreviations: [bot]tle, [cap]sule, [pil]l, [too]thbrush, [woo]d.

211 also suggests that the performance of a downstream model, such as a detector of manufacturing
 212 flaws, may be severely degraded. This is confirmed in Table 3 where we report per category
 213 and averaged F1 scores before and after modifying the resizing algorithm (columns ‘original’
 214 and ‘deployed’). In particular, we observe that D2Neighbors’ F1 score drops significantly after
 215 the resizing change, and this effect is generally consistent across categories. In particular, we
 216 observe a severe performance degradation on the ‘wood’ category, which can be explained by the
 217 spatially widespread presence of high-frequency artifacts in the original conditions (cf. Fig. 8).

218 Furthermore, the effect of antialiasing varies between different norm configurations in the
 219 D2Neighbors models. The ℓ_1 -norm variant, which has a higher overall exposure than the ℓ_2 -norm
 220 variant, sees its F1 score drop from 0.93 to 0.74 after antialiasing is introduced. Again, the wood
 221 category is severely affected, but even more so the capsule category, where the fine asperities of
 222 the surface on which the capsule is placed cause high frequency noise all over the image. Note,
 223 however, that since the anomalies for the capsule category are more spatially confined than those
 224 for the wood category, the ℓ_2 and ℓ_4 -norm variants of D2Neighbors perform comparatively much
 225 better after deployment due to their pixel-sparsity mechanism. The ℓ_4 -norm variant generally
 226 shows the strongest resilience across all categories, with an average F1 score that drops from
 227 0.91 to a less severe 0.83.

228 The difficulty of the D2Neighbors model in providing anomaly scores that generalize to
 229 changing data conditions also occurs in PatchCore, where we observe a decrease in the F1 score
 230 from 0.92 on the original data to 0.85 after deployment. This is significant because D2Neighbors
 231 and PatchCore are very different in structure. The latter extracts features using a pre-trained
 232 WideResNet50 before computing distances, and applies spatial max-pooling to identify the region
 233 in the image that is most responsible for the anomaly, building invariance to the other regions.

234 The effect of these structural differences can be seen by looking at the F1 scores per category.
235 In contrast to D2Neighbors, PatchCore experiences the largest decrease in performance for the
236 ‘toothbrush’ class (from 0.89 to 0.64). A possible explanation is an amplification/suppression effect
237 in the PatchCore feature extractor, similar to those found in CLIP, SimCLR, and BarlowTwins.
238 Specifically, PatchCore reacts strongly to hair pattern of the toothbrush, and the very thin
239 anomaly-causing bent hairs no longer find their way through PatchCore’s feature extractor after
240 being weakened by antialiasing.

241 The Clever Hans effect, where models exploit spurious correlations rather than robust patterns,
242 manifests as overfitting to high-frequency noise in training data, leading to poor generalization
243 on anti-aliased test images. In the main paper, we demonstrated the significant performance
244 degradation of CH models under changing data conditions and provided detailed results in
245 Table 3. We then proposed a simple but effective CH mitigation strategy consisting of inserting
246 a pre-processing layer at the input of each anomaly detection model that performs an 11x11
247 Gaussian blur. Note that the architecture modification is made before training, so that the data
248 is systematically blurred during training and testing and also after deployment. The blurring
249 layer is designed to reduce the model’s response to high frequency noise while maintaining its
250 response to low- and mid-frequency patterns. The effect in terms of F1 score of CH mitigation is
251 shown in Table 3.

252 We observe an improvement in performance on the deployed test set across all models and
253 categories. For example, D2Neighbors ℓ_2 recovers from 0.80 to 0.93 with CH mitigation. The
254 per-category F1 scores show that the performance recovery is systematic across all categories,
255 and even outperforms the original model for the ‘toothbrush’ category. This last result suggests
256 that blurring also improves D2Neighbors’ ability to represent anomalies. Applying the same blur
257 filter to the input of PatchCore, we observe that the F1 score jumps from 0.85 to 0.96. Again,
258 this is a significant improvement over the original performance of 0.92. One hypothesis is that
259 the blurred images propagate better through PatchCore’s feature extraction layers, allowing a
260 finer anomaly detection model to be built than the one built on noisy images. Overall, these
261 results highlight the effectiveness of CH mitigation in improving both average and per-category
262 accuracy for all models tested.

263 References

- 264 [1] S. Eslami, C. Meinel, and G. de Melo, “PubMedCLIP: How much does CLIP benefit visual
265 question answering in the medical domain?” In *EACL (Findings)*, Association for Computational
266 Linguistics, 2023, pp. 1151–1163.
- 267 [2] X. Wang, Y. Peng, L. Lu, Z. Lu, M. Bagheri, and R. M. Summers, “Chestx-ray8: Hospital-scale
268 chest x-ray database and benchmarks on weakly-supervised classification and localization of
269 common thorax diseases,” in *2017 IEEE Conference on Computer Vision and Pattern Recognition
270 (CVPR)*, IEEE, 2017.
- 271 [3] J. P. Cohen, P. Morrison, L. Dao, K. Roth, T. Q. Duong, and M. Ghassemi, “COVID-19 image
272 data collection: Prospective predictions are the future,” *arXiv 2006.11988*, 2020.
- 273 [4] K.-R. Müller, S. Mika, G. Rätsch, K. Tsuda, and B. Schölkopf, “An introduction to kernel-based
274 learning algorithms,” *IEEE Transactions on Neural Networks*, vol. 12, no. 2, pp. 181–201, 2001.
- 275 [5] L. van der Maaten and G. Hinton, “Visualizing data using t-SNE,” *Journal of Machine Learning
276 Research*, vol. 9, pp. 2579–2605, 2008.
- 277 [6] S. Bach, A. Binder, G. Montavon, F. Klauschen, K.-R. Müller, and W. Samek, “On pixel-wise
278 explanations for non-linear classifier decisions by layer-wise relevance propagation,” *PLOS ONE*,
279 vol. 10, no. 7, e0130140, Jul. 2015.
- 280 [7] G. Montavon, A. Binder, S. Lapuschkin, W. Samek, and K.-R. Müller, “Layer-wise relevance
281 propagation: An overview,” in *Explainable AI*, ser. Lecture Notes in Computer Science, vol. 11700,
282 Springer, 2019, pp. 193–209.

- 283 [8] T. Chen, S. Kornblith, M. Norouzi, and G. E. Hinton, “A simple framework for contrastive learning
284 of visual representations,” in *ICML*, ser. Proceedings of Machine Learning Research, vol. 119, 2020,
285 pp. 1597–1607.
- 286 [9] T. Chen, S. Kornblith, K. Swersky, M. Norouzi, and G. E. Hinton, “Big self-supervised models are
287 strong semi-supervised learners,” in *NeurIPS*, 2020.
- 288 [10] J. Zbontar, L. Jing, I. Misra, Y. LeCun, and S. Deny, “Barlow twins: Self-supervised learning via
289 redundancy reduction,” in *ICML*, ser. Proceedings of Machine Learning Research, vol. 139, 2021,
290 pp. 12 310–12 320.
- 291 [11] A. Radford *et al.*, “Learning transferable visual models from natural language supervision,” in
292 *ICML*, ser. Proceedings of Machine Learning Research, vol. 139, 2021, pp. 8748–8763.
- 293 [12] S. Ren, K. He, R. Girshick, and J. Sun, “Faster r-cnn: Towards real-time object detection with
294 region proposal networks,” *Advances in neural information processing systems*, vol. 28, 2015.